Development of a Deep Learning Framework for Assisting in Image-Guided Thermal Ablation of Kidney Tumors

By

Álvaro Franco González

B.Eng., Universidad Carlos III de Madrid, 2023

Thesis

Submitted in partial fulfillment of the requirements for the Degree of Master of Science in the Graduate Program of Biomedical Engineering at Brown University

PROVIDENCE, RHODE ISLAND

MAY 2025

AUTHORIZATION TO LEND AND REPRODUCE THE THESIS

As the sole author of this thesis, I authorize Brown University to lend it to other institutions for the purpose of scholarly research.

Date_____ _____
Alvaro Franco, Author

I further authorize Brown University to reproduce this thesis by photocopying or other means, in total or in part, at the request of other institutions or individuals for the purpose of scholarly research.

Date_____ _____
Alvaro Franco, Author

This thesis by Álvaro Franco González is accepted in its present form by the Center of Biomedical Engineering, School of Engineering and Division of Biology and Medicine as satisfying the thesis requirements for the degree of Master of Science.

Date_____ Signature: _____

Dr. Benjamin Kimia, Advisor

Date_____ Signature: _____

Dr. Joseph J. Crisco, Reader

Date_____ Signature: _____

Dr. Zhicheng Jiao, Reader

Approved by the Graduate Council

Date_____ Signature: _____

Dr. Marissa Gray, Biomedical Engineering
Master's Program Director

Acknowledgements

I would like to thank my family for their constant care, support, and encouragement. My father for always pushing me to my limits, knowing that I could achieve more, my mother for always being my rock, and my brother, who is and always will be my role model.

To every new friendship nurtured in Providence, despite my constant complaints about the city, for making it a delightful and important experience in my life. To my lifelong friends, who despite the distance have been pushing me.

To my professors during these two years, which havbe made my experience at Brown University a turning point in my career. But especially, I want to thank Professor Benjamin Kimia, for entrusting me with this project and guiding me thorughout. And to Cole Foster, who has been with me along the way, helping me in troubled times, solving all of my doubts, and coming up with some ideas I hadn't thought about.

Contents

List of Figures

List of Tables

Abstract of Development of a Deep Learning Framework for Assisting in Image Guided Thermal Ablation of Kidney Tumors, by Alvaro Franco Gonzalez, Sc.M., Brown University, May 2025

Renal cell carcinoma (RCC) is a life-threatening form of cancer causing tens of thousands of deaths in the USA yearly. Current treatment solutions mainly rely on partial or total nephrectomy, significantly reducing urinary function. Alternative treatments include ablation, a minimally invasive procedure that spares healthy tissues by directly applying energy to the tumor, reducing the toll on metabolic function. Ablation still remains underutilized due to the high recurrence suffered by patients. In this project, we study the viability of improving treatment procedures and outcomes of image-guided thermal ablation (IGTA) via deep learning algorithms. We make use of convolutional neural networks for the semantic segmentation of structures relevant to the disease (kidneys, tumors, and cysts), to automate the localization of the treatment zone. We make use of publicly available databases from the University of Minnesota, KiTS 19' and KiTS 23', and a private dataset provided by a team from Johns Hopkins University, to study the performance on pre- and intra-procedural image series. Our model demonstrates that it is a viable pipeline to assist in IGTA.

Chapter 1

Introduction

Despite advances in cancer diagnosis and treatment in recent decades, it still is one of the leading causes of death worldwide. Among the different kinds of cancer, renal cell carcinoma (RCC) is in the spotlight because of the need to improve treatments, given the rise in the number of cases. Traditional treatment involves surgical resection of the kidney, or a section of the kidney, that has cancerous tissue. This procedures are called radical and partial nephrectomy, respectively. Surgical procedures are declining because of the complications associated to the process. The alternative treatment for many cases of RCC relies on thermal ablation of the tumor, reducing or completely eradicating the cancerous cells in the patient, reducing the harm to the patient to a few punctures. This is a much needed improvement given that patient survival has been linked to the number of remaining nephrons after surgery [1]. The advantages posed by this alternative treatment are not restricted to safer procedures, reduced risk of complications, and shorter recovery times for the patient, as it is also a cost-effective solution that uses image-guidance to ensure patient safety. Despite the number of benefits offered by ablation, it isn't generally used because if the high recurrence rates [2]. This recurrence is caused by the wrong estimation of ablation zone and the lack of awareness of treatment extent, causing misjudgement of the situation.

In light of these challenges, this project explores the possibility of complementing this procedure with deep learning to enhance physician comprehension of the conditions of the patient. Specifically, we focus on developing an AI-assisted segmentation pipeline capable of accurately identifying kidneys, tumors, and cysts within medical images, thereby providing crucial real-time support during thermal ablation interventions. The ultimate goal would be to implement it in the clinical pipeline, so that surgeons could localize all the important

structures before, during, and after the procedure, and assess the extent of the treatment in real-time. To achieve this, we use certain deep learning models that have proved to be useful and accurate in medical imaging segmentation tasks, like convolutional neural networks, and specifically U-Nets. These segmentations aim to assist clinicians during IGTA by offering enhanced visualization and facilitating better pre-operative and intra-operative decision-making.

To fulfill our purpose, we use and rigorously test the nnU-Net framework, a self-configuring segmentation method that has become a standard benchmark in medical image segmentation, getting the best results in the Kidney and Kidney Tumor Segmentation (KiTS) challenges. It generates a 3D volumetric U-Net tailored to the input dataset, after running a standardized pre-processing. We have used several databases for training and testing, both public and private. The public databases used are KiTS19' and KiTS23', both used for the KiTS challenge in different years. The former, which included contrast-enhanced CT images and the corresponding segmentation of kidneys and tumors for 210 patients, was used for training and testing. The latter, the KiTS23' database, contains contrast-enhanced CTs for 489 patients, with the difference that this dataset includes segmentations for kidneys, tumors, and cysts. Additionally, the private database was acquired thanks to collaboration with professionals from Johns Hopkins University. This database includes an assortment of contrast and non-contrast CTs, MRIs, and intra-ablation CTs, with no segmentations. This allows us to work with two carefully curated databases, and another that contains all of the images as physicians truly work with.

We test different configurations and training procedures to find the best model for our application. Training and testing on the KiTS23' database (more complete), the best configuration resulted to be the 3D full resolution, with a 94.3% Dice score on the kidneys, and a 79.5% on the tumor segmentation predictions. Overall, the training and testing on the KiTS19' database rendered the best results, with 96.2% and 84.3% Dice scores for kidney and tumor segmentations respectively. Morevover, a qualitative assessment of the predictions on the JHU database was carried out, with the addition of computing the metrics for a few of the cases against a hand-made segmentation. We found out that the inclusion of cyst class in the segmentation reduced performance due to the difficulty in differentiating cysts and tumors. Also, we tested our model, only trained on contrast-enhanced CTs on non enhanced

CTs and MRIs, and found out that the knowledge acquired by our model is not transferable to other imaging modalities.

In this work, we have proven that our method has the potential to aid in the clinical setting by automating the segmentation for IGTA patients, reducing manually-induced bias and reducing the time spent by professionals in such a time-consuming task. By improving the accuracy of the segmentations in different instances, we will be able to improve the spatial understanding of physicians during the ablation procedures, and expect to reduce recurrence rates and improve patient outcomes. Despite our results, we understand that an improvement in accuracy, mainly in tumor recognition, is necessary before this framework can be translated into the clinical environment. Furthermore, our project aligns with ongoing trends in personalized medicine, precision oncology, and smart interventional radiology. It highlights how technology can bridge the gap between diagnostic imaging and therapeutic action, ensuring safer, faster, and more effective treatments.

Chapter 2

Background

2.1 Cancer

Although usually considered a disease, cancer has been lately described as a group of diseases that cause abnormal growth in the cells of an organism [3]. According to the American Cancer Society (ACS), there were 2,001,140 new cases of cancer diagnoses among the American population in 2024 [4]. This number is expected to grow, as it has done in previous years, as the ACS predicts 40,000 more cases in the year 2025 [5].

The changes in the genetic code are called mutations, in which the base pairs of the DNA sequence of a cell are disrupted. Mutations can appear as a result of several factors, some being random replication errors (1 base pair error in each 10^{10}) [6], by exposure to external factors, or the so-called carcinogenic agents. Carcinogens come in different shapes, but the most evident to the general public are chemical agents like tobacco. Such agents induce mutations in the DNA due to their oxidizing power, creating chemical species called free radicals, that have a huge chemical reactivity [7] and interact with the DNA strands.

The mutations needed in a cell's genome to become cancerous are unclear, as it depends on which genes are affected. After being hinted at by Kane et al. [8], it is now believed that cancer applies the two-hit hypothesis. Given the two copies of the chromosomes inside each cell, there needs to be mutations on both chromosomes to promote a cell into a carcinogenic or harmful state. Furthermore, a given mutation could even have no repercussions on the behavior of the cell, as there are regions of the DNA that do not encode proteins. However, some genes have bigger roles in the regulation of cancer, known as tumor suppressor- and proto-oncogenes [9]. The former regulates the inhibitory cell mechanisms, restricting the

proliferation of cells that contain errors in their genetic code until some mutation turns it off. One of the ways in which these tumor suppressor genes work is by unlocking programmed cell death (apoptosis) in the cells that have sustained significant genetic damage. Meanwhile, the proto-oncogenes are the ones that have a stimulatory response, become activated by some mutation, and promote the proliferation of cancerous cells.

Each tumor is classified according to the TNM system, to give a quick understanding of the condition. Tumor (T) refers to the size and ranges between 0 to 4. The value increases with size and intrusiveness to nearby tissues, with strict definitions of each value according to the affected anatomical structures [10]. As well, nodes (N) is the quantization of lymph node invasion, in the range 0-3 (seven or more infested nodes are rated as 3). At last, metastasis (M) classifies the tumors whether there exists metastasis (1) or not (0). The metastasized tissues are also taken into account, adding a letter between a, b, and c, dependent on the number of tissues that have been affected by metastasis. This classification system allows any unrelated physician to rapidly understand the evolution of the disease, without needing to analyze any tests.

All the information extracted from the TNM classification can be condensed into what is called staging. Also, any case could be directly described with this method without resorting to the TNM classification [11]. Each cancer can be assigned a stage in the range 0-4, depending heavily on the spread of the cancerous cells [10]. It is an easier way to describe the reach of the disease for the general public, offering less intricate information [11]. This classification is of great importance for the statistical study of the disease, allowing better clustering of the data.

Renal Cell Carcinoma

Carcinoma is the type of cancer affecting the epithelium, which is the tissue that forms most of the organs [12]. The kidneys are no different, and the epithelial cells are the ones that perform the most important functions in them [13]. There are several types of carcinoma, depending on the type of cells (basal, squamous, ductal, gland...) in which the tumor starts [12]. Therefore, kidney tumors are mostly gathered under the term renal cell carcinoma (RCC).

Local signs of RCC include haematuria (blood in urine), local pain, or palpable mass [14]. Other symptoms like hypertension, hypercalcemia, or erythrocytosis are more closely related to metastatic events, causing PTHrP, Renin, and Erythropoietin imbalances, respectively.

The driving event to acquire renal cell carcinoma is via von Hippel-Lindau (VHL) mutation [15]. VHL is a tumor suppressor gene, which loss causes an accumulation of HIF-family proteins, activating HIF target genes controlling angiogenesis, glycolysis, and apoptosis. But VHL mutation at 3p25 is not sufficient to induce RCC. Additionally, it has been found that RCCs typically include mutations in PBRM1, SETD1, BAP1, KDM5C, or MTOR. Some of these genes are responsible for encoding chromatin- and histone-regulating proteins, located in 3p21. This means a single copy loss in 3p will unchain the onset of RCC.

Out of the diagnosed cases of cancer in 2024 in America, 81,610 cases affected the kidney [4], and around 14,000 people died from this disease. In 2022, there were over 430,000 new cases of kidney cancer diagnosed worldwide, making it the 14th most common type of cancer[16]. It affects nearly twice as many men as it does women, which can be linked to lifestyle factors. It is important to stress the lack of diagnoses in underprivileged communities, trimming the official statistics, meaning the total number of cases and deaths might be somewhat higher.

The disparity in cases between men and women can be attributed to several factors. Among those, physical activity, food intake, and alcohol and tobacco consumption are the most significant [17]. Obesity has historically been linked to many diseases, and cancer is not excluded. High-fat diets have been proven to promote RCC, while fruits and vegetables included in diets reduce the risk of developing RCC [18]. By reducing obesity, the risk is lessened; therefore, physical activity will help in this regard, as well as reducing blood pressure and insulin resistance, which also affect [19]. Although it may seem contradictory, moderate alcohol consumption may have a positive effect on the risk of CCR [20], [21]. This effect can be split among the sexes, as beers cause this improvement in the forecast for men, but not in women. It is wine and liquor on women's cases that aid. Lastly, as a result of the carcinogenic agents in tobacco, it is known to promote many types of cancer. In the case of RCC, very high smoking intensity can be correlated to a higher risk of developing RCC [22].

Renal cell carcinoma staging is typically carried out via CT scans, allowing estimation of invasiveness, lymph node capture, and metastasis; with IV contrast enhancing the localization. Differentiation with angiomyolipomas (benign tumors) is helped due to the lack of dense fat

[14]. Due to surveillance of patients at risk, the diagnosis of RCC has seen a reduction in the average size of the tumors located, despite the higher incidence of the disease [23]. An earlier diagnosis and treatment planning result in much better outcomes.

2.2 Cancer treatments

Each patient is treated as a unique case, given that cancer can arise in different locations, forms, and tissues. Therefore, the treatment for each patient can vary enormously. Regardless, a combined approach, leveraging multiple of the following treatments, is usually the most effective strategy [24], [25]. The goal of each one of the following streams of treatment (except for surgery) is to generate cytotoxic conditions for the rapidly-dividing cells to die.

2.2.1 Chemotherapy

Chemotherapy is based on the use of chemical agents, named chemotherapeutics, traditionally targeting rapidly dividing cells and killing them [26]. This is achieved by interfering in the synthesis process of compounds like DNA and RNA [27]. Current chemotherapeutic agents exploit protein and DNA alterations of cancerous cells, avoiding occasioning damage to other dividing cells in the organism. Used chemical agents are classified according to their action and target [26]. This type of therapy is administered in several doses spaced by days or weeks [27].

Traditional chemotherapeutics tried to take advantage of the enhanced permeability and retention effect to reach any location in the body [28], given the physiological consequences of cancer. This could cause accidental damage to other body tissues, like bone marrow, which has rapid cell division. Spermatogenesis, a process consisting of millions of cells quickly differentiating into mature cells and being replaced by new cells, is completely cut off by chemotherapeutics, taking a toll on the patients [29]. Many side effects can be derived from accidental damage in chemotherapy, like pain, nausea, diarrhea, and a depressed immune system (caused by damage to bone marrow) [30].

2.2.2 Immunotherapy

With a high level of specificity, immunotherapy offers a very good option for cancer treatment [31]. This is attributed to the molecular specificity of the agents used, as they are targeted to

the kind of tumor developed. Nevertheless, it is this very specificity that makes it a more expensive and scarce treatment, requiring a more difficult production [31]. Its working principle is to enhance or restore the immune response towards the cancer cells [32]. The complexity of the processes mediated and modified in such treatments can be seen in Figure 2.1.

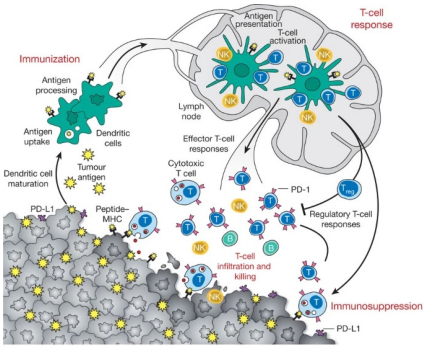

Figure 2.1: Diagram of molecular interactions in a given immunotherapy treatment [33].

2.2.3 Surgery

Surgical procedures involve some tissue from the patient being removed, added to, or even remodeled. In oncology cases, it is the tumor (or a part of it) that is being removed, like in Figure 2.2. This is usually referred to as resection surgery, in which the tumor is more or less solid and allows for surgical removal [34].

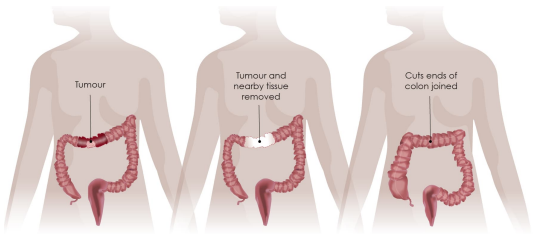

Figure 2.2: Resection surgery drawing for bowel cancer [35].

Although the outcome of resection surgery can be enough to remove a localized tumor completely, many cases require a more advanced approach. Frequently, surgery is combined with other treatments like chemotherapy or radiotherapy. The latter may be supplied before, during, or after the surgery. In recent times, surgery is moving towards minimal invasiveness, given the advantages it poses. Reduced post-operative rest, scarring, mid-operation

complications, and risk of bleeding are some of those advantages. The downside of these procedures is the lessened awareness of the treatment extent.

2.2.4 Radiotherapy

Although the term is generally used for any radiation of a tumor with the aim of eradicating those carcinogenic cells, radiotherapy explicitly refers to external beam radiotherapy (EBRT) or teletherapy. On the other hand, radiation applied from an internal source is referred to as brachytherapy [36]. This process can be carried out with x-ray or gamma photons, electrons, protons, neutrons, or even alpha particles [37]. A linear accelerator accelerates these species to reach the desired dose energies. Ionization achieves the ultimate goal of extinguishing cancerous cells by damaging the cells' DNA [37]. Cellular repair mechanisms are typically capable of fixing DNA damage to a certain extent. However, when the damage is extensive, cells become unable to replicate and go into senescence.

Generally, radiation therapy is provided externally, so it traverses healthy tissues on its path to the tumor in cases where the tumor is not on the surface. To guarantee that enough radiation reaches the tumor, the energies used are in the megaelectron-volt range [38]. This magnitude is much higher than what is used in imaging, but it helps to quickly eradicate the tumor. Still, several sessions of radiotherapy are usually required for each treatment. The primary challenge in radiotherapy is striking a balance between maximizing radiation to target malignant tissue while preserving healthy structures to the greatest extent possible [39].

One of the possibilities of radiation therapy is to deliver the radiation dose during a surgical procedure. In this kind of procedure, the tumor is resected as much as possible [40]. Afterward, any remnants are irradiated, as well as the so-called tumoral bed. The tumoral bed is the boundary between the tumor and healthy tissue, which might still have tumorigenic cells or factors that might be able to induce cancer in the future. The benefits of the intra-operative counterpart over conventional radiotherapy are better protection of the healthy tissues and more direct radiation of the tumor. By rearranging and shielding the surrounding organs [40], a better sight of the tumor can be achieved.

2.2.5 Image-Guided Ablation

The term ablation is used to refer to cancer treatments directly applying chemical or energy-based therapies with the goal of substantially minimizing tumors [41]. Most of these therapies are performed with radiological aid, hence the image-guidance. These procedures have often been deemed as minimally invasive, which is the reason for their popularity lately. The energy-based ablation methods include thermal and nonthermal techniques. The thermal approach involves either heating or freezing the tumor, until cytotoxic conditions are reached. Heating is achieved via laser, radiofrequency, microwave (grouped inside radiofrequency as its bandwidth, 300MHz - 300GHz, is inside the RF spectrum, 3KHz-300GHz), or ultrasound, depending on the case [42]. The cold approach is named cryoablation, and involves the expansion of a cryogen at the probe's tip, causing heat transfer [41].

The use of imaging for guidance can be used at many steps during the procedure (planning, assessment, intra-procedural...) and helps in achieving better and safer results [43]. A combination of different imaging modalities allow for better results by harnessing the information provided by each. Typically, pre-procedural imaging (CT or MRI) can be registered with real time intra-procedural imaging (like ultrasound) to locate the structures of relevance during the procedure. As well, imaging performed after concluding the procedure is useful to evaluate the treatment and assess its effectiveness.

2.3 Medical imaging

A medical image is a depiction of (a part of) an organism created by the measurement of a certain physical characteristic. There are several modalities (some shown in Figure 2.3) according to the principles on which they are based [44]. In radiographic techniques, images are acquired based on photon attenuation by the traversed tissues [45]. On the other hand, ultrasound imaging relies on the evaluation of acoustic impedance and attenuation to generate the image [46]. Lastly, magnetic resonance imaging (MRI) manipulates the spin of protons inside the body to create the image [47]. MRI surpasses CT in its ability to visualize soft tissue, but it is not as effective in imaging hard tissue. The final image is an ordered set of values, which, correctly ordered, represent a section of the body.

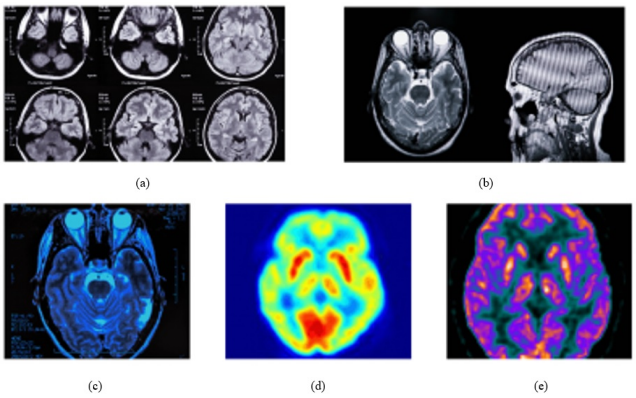

Figure 2.3: Examples of images from different modalities, (a) and (b) are MRI, and (c), (d), and (e) are nuclear imaging techniques [48].

In this work, we have focused on Computed Tomography (CT) and Magnetic Resonance Imaging (MRI). A detailed explanation of both techniques is provided in sections 2.3.1 and 2.3.2.

2.3.1 Computed Tomography

For more than one century, x-ray imaging was used in clinical settings for the diagnosis of diseases, but lacked depth information. It was in 1972 that Hounsfield created the first CT scanner [49], for which he received the 1979 Nobel Prize in Medicine, shared with Allan Cormack. Its working principle is the revolution of the x-ray technology around a central axis while keeping the patient inside of the circumference created by the turns, like in Figure 2.4(a).

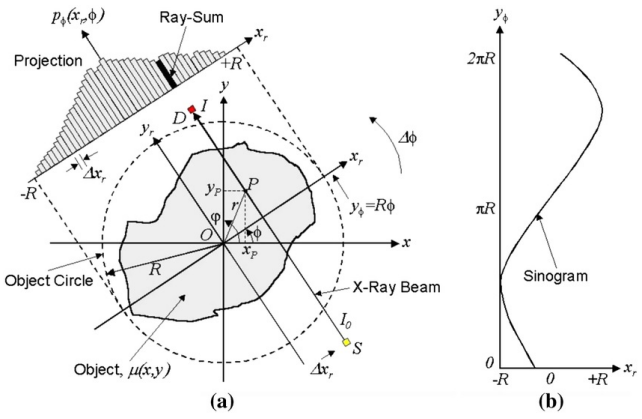

Figure 2.4: Schematic of the functioning of a CT system. (a) represents the image acquisition in each position, (b) is a sample sinogram for a given point. [50]

There is a circuit with a resistive component that releases electrons via thermionic effect due to the heat generated by the current [51]. Those electrons are accelerated with a voltage difference created between the heated filament (cathode) and a spinning disk made of metal (anode). Due to the voltage [52], the electrons hit the anode, generating a beam of photons. The materials of the cathode and anode depend on the type of image and photon energy desired, but are typically made of Tungsten [53]. These photons are created through two different processes: Bremsstrahlung, and characteristic radiation. The former generates photons due to the braking and deviation of the electrons due to electrostatic force as they get closer to the nucleus of an atom (Figure 2.5) [54], and the latter depends on the electronic transitions of the atom caused by orbitals emptied by the incident electrons [55]. The characteristic radiation generates photons in very specific energy values (the difference between the levels involved in the transition [56]), while the Bremsstrahlung radiation energy depends on the energy loss of the electrons. All of this generates a polychromatic energy spectrum, although it can be filtered with sheets of metal to reduce the energy of the photon beam [57] or remove the peaks of the characteristic radiation.

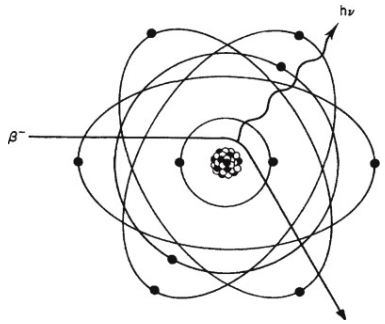

Figure 2.5: Schematic of the kinematics involved in Bremsstrahlung [58].

The image will be formed by the photons that can get through the body of the patient and reach the detector behind. Therefore, there is a measurement of the absorption and attenuation of photons along the body [59]. The interaction of those photons and the atoms inside the patient shapes the image that will be formed, and is defined by the photoelectric effect and Rayleigh and Compton scatter [60]. The attenuation of photons through the body can be statistically modeled by the Beer-Lambert law as in Eq. 2.1, which depends on the linear attenuation coefficient of the tissues traversed by the photons [61].

$$N = N_0 e^{-\mu x} \tag{2.1}$$

The attenuation maps obtained in each shot are radiographies, and they are mathematically processed via filtered backprojection [62], radon transform [63], iterative reconstruction, or other methods to generate the 3D image of the whole body. With the 3D volume, a radiography in any desired direction can be computed. Lastly, the intensity of any CT is remapped to a known scale for standardization, in which water has a value of 0 and air is -1000, called Hounsfield units (HU) [64].

2.3.2 Magnetic Resonance Imaging

Magnetic resonance imaging is based on the excitation of the nuclei inside the human body, mainly hydrogen atoms. A strong magnetic field, typically $3T$ (for comparison, Earth's magnetic field is of the order of $50\mu T$ [65]), is generated by superconducting coils. Different image acquisition means the information that is depicted in such images is different than what CT provides. Also, the biggest advantage MRI poses is the use of non-ionizing energy, making it much safer to use. Paul Lauterbur and Peter Mansfield received the Nobel Prize in Medicine for the development of this technology in 2003 [66].

$$\gamma = \frac{|\vec{\mu}|}{|\vec{L}|} \tag{2.2}$$

Following Maxwell's equations of electromagnetism, a magnetic field will be created in the center of a coil through which an electric current is flowing [67]. This is how the magnetic field in a MRI scaner is generated. To get to the high values of the magnetic field that is needed for this kind of images, the current through the coil has to be of great intensity. That's the reason for using superconductors, in which the electrical resistance is negligible. A superconductor is a material, typically ceramic, that exhibits no electrical resistance when exposed to temperatures below a critical point (around 80K). In order to achieve superconductivity inside an MRI machine, liquid nitrogen is used for constant cooling [68].

$$\omega_0 = 2\pi f_0 = \gamma B_0 \tag{2.3}$$

Atomic nuclei inside the magnetic field will align their intrinsic spin with the direction of the magnetic field [69]. But this will only happen for atoms with an odd number of protons and/or neutrons. These atoms will be characterized by their gyromagnetic constant, which

relates their angular and magnetic moments, as seen in Eq. 2.2. When aligned, the nuclei will be in a state called Larmor precession, and the frequency is given by Eq. 2.3. These nuclei will have two possible states, depending on the alignment. The low energy state, is parallel to the magnetic field direction, which is considered the "spin up" position. The high energy state, the antiparallel alignment, is also the "spin down". The nuclei will randomly distribute among both states, which will be separated by an energy gap. Transitions can happen between both states, as the energy gap is defined as Eq. 2.4. There is a difference in "up" and "down" populations, as the lower energy state is more favorable. This difference in populations is approximated by Eq. 2.5.

$$\Delta E = \gamma B_0 \tag{2.4}$$

$$\frac{N_{up}}{N_{down}} = e^{\Delta E/kT} \tag{2.5}$$

The superposition of all the nuclei magnetic moments will give a total magnetization vector. For such, we will consider the longitudinal and transversal components [70]. Inside the magnetic field, without any further manipulation, there will be no transversal component, given that all the nuclei cancel themselves out. For the longitudinal component, that is parallel to the magnetic field, it can be calculated by Eq. 2.6. This will be the spins resting state.

$$\overrightarrow{M} = \frac{1}{2}(N_{up} - N_{down})\gamma \tag{2.6}$$

Due to resonance, if these nuclei are hit with an EM wave (RF spectrum) which energy is exactly the gap between "up" and "down" states, they will lose their alignment. This is called a 90º pulse, and causes the total magnetization vector to rotate from the longitudinal direction into the transversal plane. It takes some time for the spins to recover their resting state. This recovery, described by the Bloch equation in Eq. 2.7 [71], is measured in two different ways.

$$\frac{d\overrightarrow{M}(t)}{dt} = \gamma(\overrightarrow{M}(t) \times \overrightarrow{B}(t)) - \frac{M_x(t)\hat{e}_x + M_y(t)\hat{e}_y}{T_2} - \frac{(M_z(t) - M_0)\hat{e}_z}{T_1} \tag{2.7}$$

Firstly, the longitudinal relaxation, dependent on the spin-lattice interaction. The recovery of longitudinal magnetization is characterized by the value T_1, which is a measure of the energy exchange between the excited nuclei and the surroundings (lattice). It is modeled by Eq. 2.8. This T_1 value will depend on the magnetic field intensity, and is lower for solids.

$$M_z = M_0(1 - e^{-t/T_1}) \tag{2.8}$$

The second process is the transverse relaxation, or spin-spin interaction. This is the demagnetization in the transversal plane, characterized by T_2, as the individual spins start to precess and de-synchronize. This represents the reorganization of the spins, which only depends on the atoms considered, and is represented by Eq. 2.9.

$$M_{xy} = M_0 e^{-t/T_2} \tag{2.9}$$

Spatial encoding is performed by applying gradients of the magnetic field, so that atoms in different regions of the body will have different resonance frequencies. Different coils will be situated around the patient, and will receive the signals from the magnetization. From those signals, different images can be formed [47]. The most typical are T1-weighted and T2-weighted, in which the tissues are depicted according to their T_1 and T_2 times, respectively.

2.3.3 Segmentation

The aim of image segmentation is to sort the pixels of the image into groups of shared characteristics [72]. In the case of medical imaging, it is used to localize organs, lesions or other regions of interest, differentiating them from the background [73]. This task is usually carried out by expert physicians, which is a time-consuming task. It is affected by subjectivity, as different doctors might have different criterions for segmenting. There are automated and semi-automated pipelines that make the process more efficient, and reduce bias generated by human decisions. Lately, artificial intelligence has taken over these tasks, offering quick and reproducible algorithms[74]. The bias in AI-assisted segmentation will be dependent on the bias of the training dataset on which the algorithm is trained on.

This technique helps doctors to increase their awareness and knowledge of each case. From this information, 3D models can be created, allowing a more intuitive understanding

of the patient's anatomy in three dimensions. It is useful for diagnosing diseases, treatment planning, or even disease monitoring to study progression and treatment response.

2.4 Artificial intelligence

Artificial intelligence can be defined in several ways. For one of the pioneers of the field, Marvin Minky, artificial intelligence is giving machines the ability to perform tasks that require human intelligence. From the Turing test perspective, it is the ability of machines to not reveal they are machines while communicating with humans[75]. But the term was first coined at the 1956 Dartmouth Summer Research Project by John McCarthy.

For computers to achieve intelligence, there has to be "learning". From the input data perspective, there are several types of learning [76]:

- Supervised learning: these algorithms assume the model is trained on data similar to the task at hand [75]. They have train and test sets, and the algorithm will learn patterns from the given outputs of the train dataset. Then, it will make predictions on the test set matching what was learned previously.
- Unsupervised learning: these do not need assistance, as they will learn from the unannotated data that was given. It learns features from the input to recognize patterns.
- Semi-supervised learning: combines the abilities of both for leveraging small sets of labeled data, predicting over new unlabeled data, and adding them to the training data.
- Reinforcement learning: algorithms that learn through trial and error according to a reward function, by interacting with the environment and receiving feedback.

There are other kinds of classifications inside artificial intelligence, which depend on the algorithm design. Machine learning is considered to be the development of algorithms enabling learning from data without explicit programming. There is a subset of machine learning, named deep learning, that uses artificial neural networks to simulate human learning. The first neural network was developed in 1943 by neuropsychologists McCulloch and Pitts, mimicking the behavior of neurons [75].

Depending of the architecture and features used in the neural networks, they will belong to different classes. The simplest models are made of "dense" layers stacked on each other. The stacking of these layers, each learning linear relationships, allows the whole network to

learn non-linear relationships between input and output. The predicted output is evaluated by a cost function, defining the distance to the target output [77]. This distance is minimized, via back-propagation, until the network finds an optimal configuration.

More complex architectures try to leverage data organization, like convolutional neural networks or graph neural networks [78]. Others revolve around repeating data items, calculating probabilities according to those repetitions, like recurrent neural networks. These kinds are also used in language processing, which is improved by the use of transformers and attention modules. Both convolutional networks (CNNs) and transformers are used for computer vision tasks like image classification and object recognition.

Lately, the use of Generative AI has skyrocketed, intending to create new data rather than learn relationships between input and output [79]. They can even convert one type of data into another [80]. This is achieved by an algorithm understanding patterns and structures from the training set, and being able to generate novel data. One kind of architecture used in Gen-AI are Generative Adversarial Networks, which is actually the coupling of two different neural networks that compete against each other. Another kind is variational autoencoders, which encode the input data into a latent space representation, from which a decoder can extract data in the shape of the input. More models used for GenAI are transformers and diffusion models.

There is a special kind of convolutional neural network that is heavily used for medical imaging, which is the U-Net [81]. It uses a combination of 2D convolutions and pooling to downsample the input images several times, before reaching the middle layer. The result after the middle layer is upsampled by the reverse process, until it reaches the output. Fine features from each resolution level at the encoder branch are passed into the same-level resolution steps in the decoder, to avoid losing fine feature information. This configuration forms a shape resembling the letter U, as seen in Fig. 2.6, which names the architecture. The convolution step is a transformation of the image in which several filters with different characteristics are passed through the image, usually to extract distinct features. In this case, the learning is done through the filters, as the algorithm learns which filters are applied in each step (downsampling, linear, and upsampling), for the input image to be transformed into a desired output.

The use of such architecture in medical imaging resides in its advantages. Firstly, the use of skip connections preserves finer details in the image that might be detrimental to the

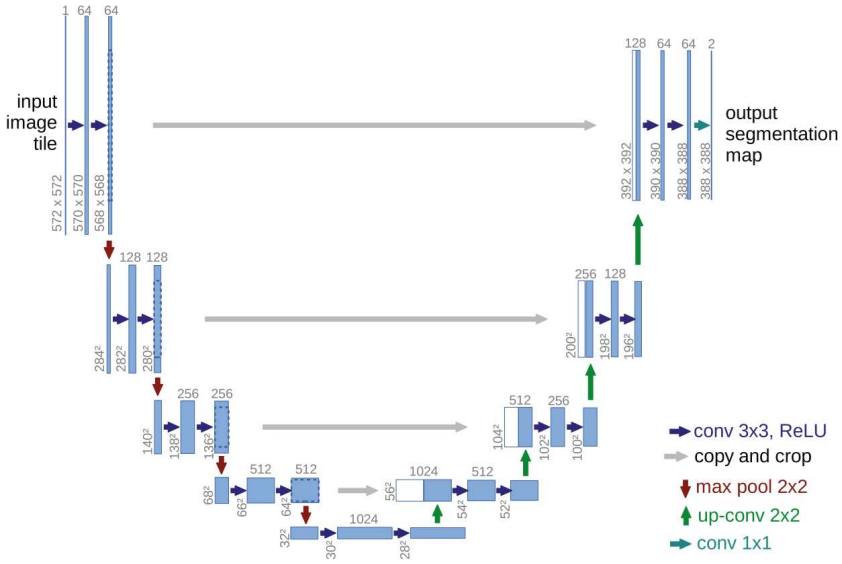

Figure 2.6: Sketch of the original U-Net, proposed in [81].

application. Secondly, these models are proven to extract patterns quickly, performing well with small datasets (common occurrence in healthcare). This architecture works with 2D images as input, establishing the relationship between the original image and a given label. But working in a healthcare environment, in many cases, the images taken from patients or test subjects come from 3D modalities, in which volumes are represented. For such cases, there are two approaches: the 3D images can be separated into 2D slices, each used as input for a U-Net; or one can use an architecture that works on a three-dimensional domain. The volumetric U-Net, or V-Net, was developed in 2016 by Milletari, Navab, and Ahmadi [82] and is just the 3D counterpart of the U-Net, using 3D convolutions and pooling functions.

Chapter 3

Related work

The first and most common method for segmenting medical imaging is manual labeling. What is currently used to set the gold-standard for other segmentation methods was decades ago the only available method in which a reliable and accurate segmentation was possible [83]. This is a highly time-consuming task that despite being currently used as ground-truth is heavily impacted by operator bias. Since the beginning of medical image segmentation, there have been different methods developed, that have been used to either segment the images or assist by refining the already existing segmentation [84].

The simplest of these methods is thresholding, which consist on clipping the intensity values in the image for selecting the region of interest. This works best for applications in which the intensity values of the organs of interest have consistent ranges. Intensity-based thresholding has advanced, with algorithms like Otsu that adapt the thresholds to the intensity distribution along the image [85]. Like many other algorithms, it works by minimizing a cost function, which in this case is dependent on the class variances. Any kind of thresholding method can be applied to whole images or small windows, therefore promoting thresholding as a post-processing method in some segmentation processes, as many organs have well-established intensity values.

A different method globally used is region-growing. It begins with the selection of a seed in the image inside your region of interest [83]. Adjacent pixels (or voxels) are checked following a pre-established criterion, and will be added to the region if the criterion is satisfied. This process is repeated until no more neighboring pixels meet the criterion. This method works for regions that exhibit homogeneous properties, and generates single-label masks.

Another common method in medical imaging segmentation is edge-detection. Considering the images as disrete-value functions, mathematical operations can be performed on them [86]. Edges are defined as steep changes on the intensity distribution, and the slope of these changes can be calculated via gradients. By establishing a threshold for the minimum slope that will constitute a significant edge, a new image illustrating the edges can be formed. This operation is typically computed by the convolution of gradient filters with the image. Among these methods, the Canny detector does not only find the gradients, but also finds the direction of the edge to label the pixels that form the principal edge [87].

Every segmentation method is susceptible to noise and artifact, which distort the images. In manual segmentation tasks, the operator can adjust its criterion to adapt to the image at hand, but that is difficult or impossible with other methods. That, added to the high reproducibility and automation, are some of the advantages that deep learning poses for medical image segmentation. Given a comprehensive database, ideally a deep learning-based algorithm should be able to copy the criterion used for segmenting. Therefore, if the training cohort has been created by manual segmentation taking into account noise and artifact, the model should be able to copy its performance.

Regarding the implementation of deep learning algorithms in medical image segmentation, the use of U-Net [81] (or its 3D counterpart, V-Net [82]) is the method that has gained the most traction in the last years. The main focus of deep-learning segmentation is for brain and tumor imaging, mainly conducted in MRI scans. Since its development in 2015, the U-Net has been one of the most cited papers in medical imaging, with over 100,000 citations. Many have implemented similar approaches or have built on them to improve the achieved results. To enhance the performance of vanilla V-Nets, we have found different additions to this method. Firstly, one of the ways to improve the segmentation results is by considering multi-resolution levels for the segmentation [88], [89]. These authors base their approach on the working principle of U-Nets, by analyzing the images at different resolution levels to extract details and descriptors at each of them. Some other authors opt for using self-assembling U-Nets, nn-UNet [88], [90]–[95], which create a network that adapts to the input.

A different approach is to use properties from transformers, like self-attention [73], [96] inside the V-Nets, to retain focus on different regions of interest inside the images. In other cases, context extractors [97] are used to salvage the loss of information caused by

convolutions and pooling, by using a pathway composed of a feature encoder, a context extractor, and a feature extractor. In other cases, the improvement is to redesign the skip connections, adding dense layers in between [98], [99], or introducing a transformer module [92]. Given the good performance of generational adversarial networks (GAN) in different applications, they have also been tested for segmentation, using the usual U/V-Nets as backbone [100]–[102]. In these, the V-Net acts as an image generator (same as before), but now there is a discriminator module that is trained against the generator, trying to find which outputs (segmentations) are ground-truths and which are generated. Lastly, using latent space representations of the images and segmentations has also rendered good results for segmentation, introducing the use of VAEs [101], [103].

Chapter 4

Materials and methods

4.1 Datasets

KiTS 2019

With no access to an adequately curated kidney tumor database, we relied on publicly available databases. We considered that the Kidney and Kidney Tumor Segmentation Challenge (KiTS) was a good place to start, as the goal was to segment the structures that are of interest for our application. Additionally, we were directed towards this database as a starting point by experienced physicians. This challenge has been held in the years 2019 [104], 2021 [105], and 2023 [106]. The original 19' KiTS testing database is available at The Cancer Imaging Archive (TCIA) [107].

At first, the 19' KiTS database, downloaded from TCIA, was used. This database contained the folders for 210 patients who had been treated at the University of Minnesota Medical Center from either partial or radical nephrectomy, and a CSV file showing age, gender, body mass index (BMI), comorbidities, smoking history, alcohol use, procedure complications, staging, histologic classification, and more fields related to surgery outcome. Each patient in this cohort was assigned a code number, going from KiTS-00000 to KiTS-00209, to avoid confidentialy problems and maintain anonimity.

The folders for each patient contain at least a contrast-enhanced pre-operative CT scan in late-arterial phase and its corresponding segmentation showing the kidneys and the tumor(s), in DICOM format. Some patients included a second pre-operative CT scan without contrast agents and/or a post-op scan. Regardless of the additional scans, there was only one segmentation for each patient, the one corresponding to the enhanced scan. The contrast-

enhanced images were referred to as "arterial", while the post-op ones are "late". The inclusion of all of these files can be seen in Fig. 4.1.

Series #	Series description	Modality	Size	Count	Date added
5	noncontrast	CT	512x512	93	2025-02-...2:12.152
7	arterial	CT	512x512	611	2025-02-...2:12.309
10	late	CT	512x512	154	2025-02-...2:11.857
300	Segmentation	SEG	512x512	1	2025-02-...2:12.147

Figure 4.1: Visualization of image series for patient KiTS0000 in 3D Slicer, containing all the available scans and segmentations.

An example of a patient CT scan and its corresponding segmentation overlying the structures of interest can be seen in Fig. 4.2. The 3D render of these segmentations can be found in Fig. 4.3. We can see how the kidney segmentation (in red) overlays the kidney, and has a green section, which is the tumor. In this database, we only have three different classes in the segmentation:

- Background: 0
- Kidney: 1
- Tumor: 2

The segmentations were performed by manual delineation on a Web application on Canvas by a cohort of medical students [108]. Users would draw contours on the transverse plane images. To reduce workload, subsampling was done to reduce the number of slices depicting the ROI. To compute the final labels, they performed interpolation to extend the labels to excluded slices. Instructions were to include renal capsule, and exclude tissues other than renal parenchyma, like the hilum, ureters, or any vessels. To refine the boundaries, intensity thresholding was performed, given that kidney tissues (HU $>$ 0) are significantly different than fat (HU $<$ 90). Images were treated with mean and/or median filters to improve image quality.

After segmentation and supervision by students, 30 images were randomly selected and segmented again by a different student. The Dice-Sørensen coefficient (DSC) between the first and the second tumor segmentation for those images was around 92%, denoting the segmentation bias that was previously mentioned for manual segmentation.

Most of the contrast-enhanced images, which will be used for working with our architecture, have dimensions of $512 \times 512 \times d$. There is only 1 patient case in which the axial slices are not in 512×512 size. There is more variability here regarding the number of axial slices,

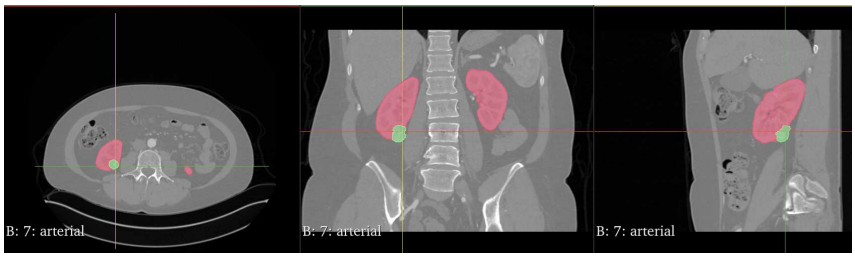

Figure 4.2: Visualization of the "arterial" contrast-enhanced CT scan and segmentation for patient KiTS0000 in the axial, coronal, and sagittal planes, via 3D Slicer.

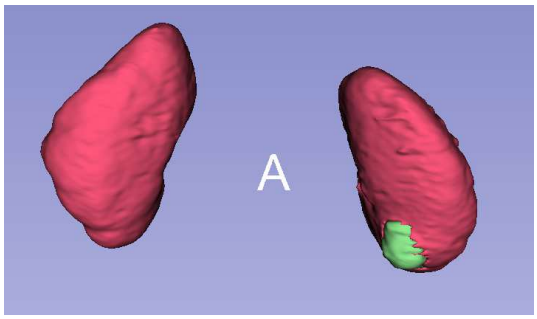

Figure 4.3: 3D render of the kidney and tumor segmentation for patient KiTS0000, in 3D Slicer.

d. The median number of axial slices for the images is 107, and we can see the distribution in Fig. 4.4a.

The variability between patient images is due to several reasons. Despite the whole database belonging to the University of Minnesota Medical Center patients, the scans were taken in different institutions. Therefore, each scan might not only come from different institutions, but also from scans made by different manufacturers, and even acquired following different protocols. The disparity in the number of axial slices might also be due to choices made by attending physicians.

KiTS 2023

After the success of the original Kidney and Tumor segmentation challenge, it was celebrated in 2021 and 2023. Given the data-intensive nature of any artificial intelligence task, improving a database is of utmost importance. Therefore, the organizers tried enhancing the provided database by including more cases and improving the available segmentations. As in the previous version, patients were given a code, to avoid confidentialy problems and maintain anonimity.

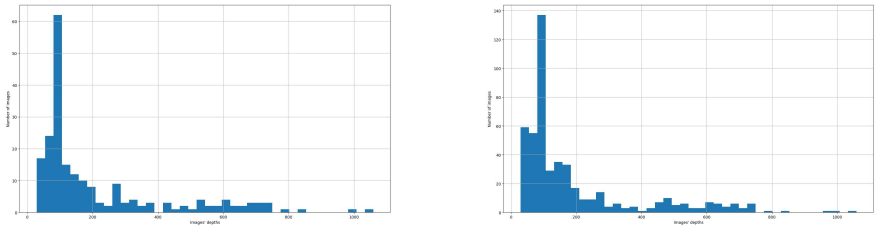

(a) Histogram of the number of axial slices of the cases in the KiTS 19' database.

(b) Histogram of the number of axial slices of the cases in the KiTS 23' database.

Figure 4.4: Histograms for the number of axial slices present in each of the imaging databases used for training.

For this edition, organizers included the original 210 cases from KiTS 19' (only contrast-enhanced CT scans) and added 278 more cases. Out of the total 488 cases, three of them had axial slice sizes different from 512×512, cases KiTS160 ($796 \times 512 \times 252$), KiTS319 ($651 \times 512 \times 81$), and KiTS325 ($632 \times 512 \times 40$). Due to the distorted nature of these images, they were excluded from the training cohort to avoid problems. We can see the distribution of the number of axial slices in Fig. 4.4b. The median number of axial slices in this database is 104.

For this database, the segmentations have been improved. Annotations are conducted on a publicly accessible, web-based platform to facilitate transparency and external scrutiny. The annotation workflow consists of sequential stages. Users can create annotations in the web, which will be reviewed by experts (radiologists and urologic oncologists). Final changes to the published segmentations are uploaded by the experts after thoughtful evaluation of annotations. In this database, we have four different classes in the segmentation:

- Background: 0
- Kidney: 1
- Tumor: 2
- Cyst: 3

Johns Hopkins archive

Due to collaboration with Johns Hopkins University's Dr. Harrison Bai, we had access to a subset of their patient database. This database is not publicly available and was retrieved

Code name	Imaging modality
intra	Intraoperative CT
pre	Non-enhanced CT or MRI
pre_V	Venous contrast-enhanced CT or MRI
pre_A	Arterial contrast-enhanced CT or MRI
pre_T1C	Contrast-enhanced T1-weighted MRI
pre_T2	Non-enhanced T2-weighted MRI

Table 4.1: Image codes given by Johns Hopkins.

after Internal Review Board approval. We received images from 103 patients who underwent image-guided cryoablation therapy for renal cell carcinoma. Those images include 108 simple CT scans, 114 contrast-enhanced CTs, 8 different MRI scans, and 119 intra-procedural CT scans. Each patient in this cohort was assigned a code number, going from JHU_0001 to JHU_0103, to avoid confidentialy problems and maintain anonymity. This code number was followed by a short code stating the type of image that was given, as per Table 4.1. Any number contained in the filenames is to differentiate between different images from the same modality.

Given the nature of intraoperative scans, the least amount of time possible is spent taking intraoperative CTs, to reduce patients and clinicians' exposure to ionizing radiation and the shortest time for the surgery. Therefore, intraoperative CTs are difficult images to take, and this was shown in the images received from JHU. Additionally, the presence of ablation probes in the body generate artifact in the images. This is caused by the material they are made of, generally metal, absorbing the photons emitted by the source and distorting the resulting image. In Fig. 4.5b we can see a case in which the image was properly formed, with a restricted field of view, not showing the whole abdomen. This is not typical, and because of the aforementioned conflicts, intraoperative CTs usually look like Fig. 4.5a.

As we said, the database from JHU also contains MRI scans of some patients. Out of the 8 MRIs, we have one T2-weighted, another contrast-enhanced T1W, and the rest were simple T1-weighted. We can see the difference between sequences in Fig 4.6.

From the total 230 pre-procedural scans, only two had different dimensions than $512 \times 512 \times d$. We have a median of 168 axial slices. The distribution of axial slices is shown in Fig. 4.7. From this patient cohort, there were at least 6 patients that only had one kidney remaining.

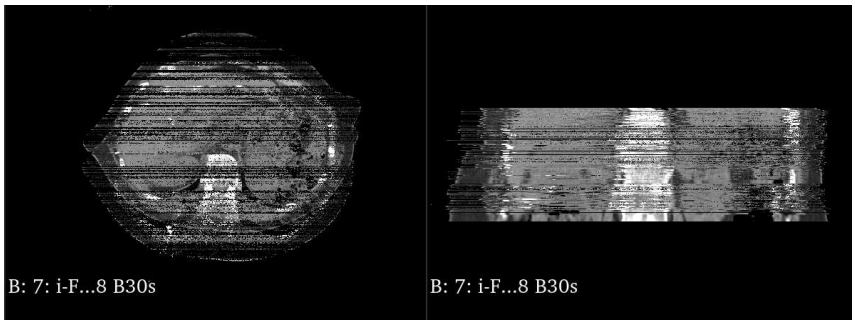

(a) Visualization of patient JHU_0040 intra-procedural CT scan from JHU.

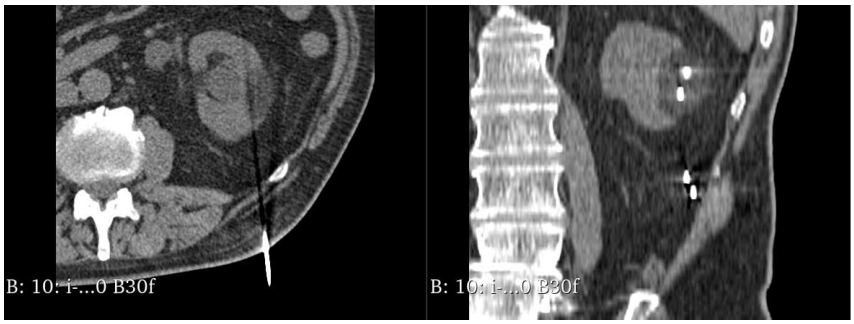

(b) Visualization of patient JHU_0103 intra-procedural CT scan from JHU.

Figure 4.5: Display of two intra-procedural CT scans from JHU database.

We changed the nomenclature given by JHU when using this imaging database in our segmentation pipeline. The correspondence between names can be found in Appendix A.

4.2 Preprocessing

To use these databases as input in a Convolutional Neural Network, we need consistent sizes among images. There are many factors to take into account when choosing a uniform size to convert all of the images. This is the reason behind resampling every image (except intra-operative CTs) in KiTS 19', KiTS 23', and JHU databases to a $512 \times 512 \times 256$ size. The selection of these numbers came from a compromise between computational cost, resolution improvement, and information loss.

Using SimpleITK, itk, and nibabel packages in Python, we converted the DICOM images from KiTS19' and JHU databases into NIfTI format, while performing interpolation to transform the original images into our desired $512 \times 512 \times 256$ size. For the KiTS23' database, we used the same packages and functions to perform the interpolation. The only difference is that the original images were already in NIfTI format and no conversion was needed. For image interpolation, we used the linear interpolation method included in

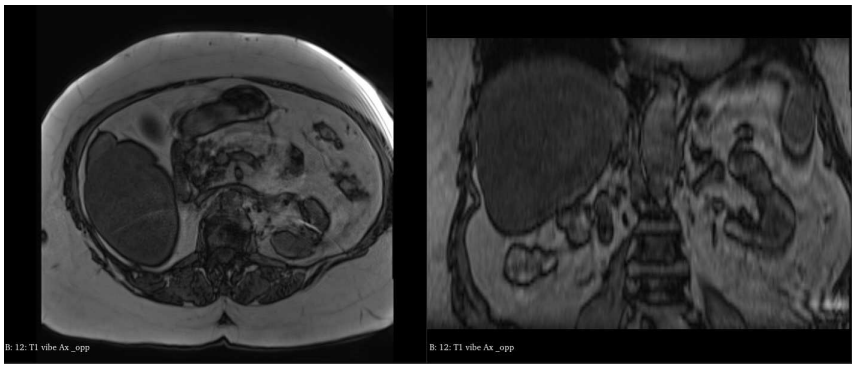

(a) Visualization of patient 13 T1-weighted MRI scan from JHU.

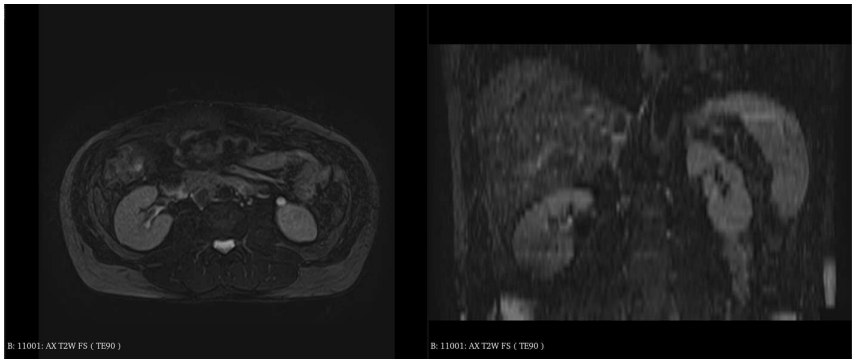

(b) Visualization of patient 82 T2-weighted MRI scan from JHU.

Figure 4.6: Comparison of MRI modalities in the JHU database.

SimpleITK to calculate the images in the new grids. On the other hand, for segmentations, we used the nearest neighbor interpolation method from itk, as we don't want intermediate values, just the classes we already had. We also performed intensity rescaling on each image to a 0-255 range.

4.3 Segmentation

In our databases with ground-truth segmentations (KiTS19' and KiTS23'), the segmentation of the kidneys are produced in such way that cortex and medulla are labeled, but generally excluding the renal pelvis. We can see those parts in Fig. 4.8. This criteria for segmentation comes from the fact that we are considering renal cell carcinoma, and the cortex and medulla are the parts of the kidney formed by epithelial cells.

After considering the current methods that have proven to perform better in similar tasks, we decided to evaluate the different configurations offered by nnU-Net. Different teams have shown their success in the Kidney and Kidney Tumor Segmentation Challenges [88],

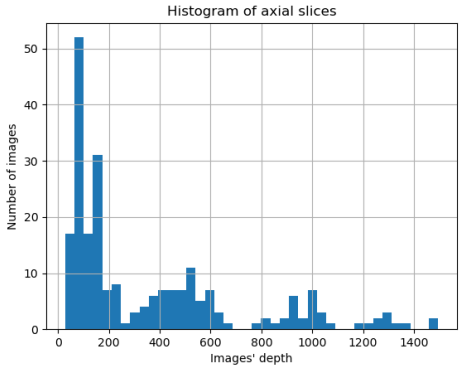

Figure 4.7: Histogram of number of axial slices of pre-procedural scans in JHU database.

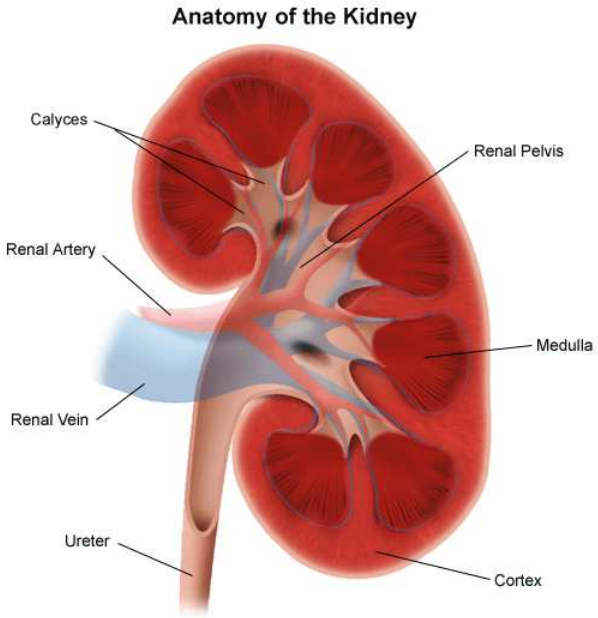

Figure 4.8: Sketch showing the anatomy of the kidney [109]

[90]–[95] using this approach. We followed the instructions at their GitHub repository to install and use this approach. This program generates a segmentation architecture around your dataset, adjusting its properties. You choose which kind of architecture you want to use from the following options: 2D, full resolution 3D, low resolution 3D, and cascade 3D.

This program also performs some preprocessing on the images. As we are using CT images, and it is specified in the dataset created for nnU-Net, nnU-Net performs intensity normalization and clipping (0.5 and 99.5 percentiles for clipping). During the preprocessing, nnU-Net already splits the dataset into training and validation sets (80-20). For training, the common characteristics for every configuration are the use of the Kaiming normal initializer,

and the choice of 1000 epochs. This program uses a combination of different loss functions, from Dice-Sørensen, categorical cross-entropy, and topK losses.

As we are training on 3D volumes, we started by training on KiTS19' database with the simpler full-resolution 3D model. When we started working with the KiTS23' dataset, instead of just trying the full resolution module, we tried with all the 3D possibilities, to find the best configuration. In order to run the cascade model, a 5-fold training on the low resolution 3D model was needed.

For evaluating the segmentation results, we used two different metrics, that are typically used in imaging tasks. For the following metrics, we will consider S_{GT} as the ground truth segmentation, and $S(x)$ as the segmentation predicted by our methods. Firstly, the Dice-Sørensen coefficient, which is calculated from Eq. 4.1.

$$DSC = 2\frac{|S(x) \cap S_{GT}|}{|S(x)| + |S_{GT}|} \tag{4.1}$$

The other metric we will use is the Jaccard index, also known as Intersection over Union (IoU), shown in Eq. 4.2.

$$IoU = \frac{|S(x) \cap S_{GT}|}{|S(x) \cup S_{GT}|} \tag{4.2}$$

These two measures are related by the following equations:

$$DSC = 2\frac{IoU}{IoU + 1} \qquad\qquad IoU = \frac{DSC}{2 - DSC}$$

Chapter 5

Results and discussion

As was explained in section 4.3, we tried different configurations of nnU-Net for the deep learning-assisted segmentation of kidneys and tumors in medical images. The accuracy of the different trained models is showcased in Table 5.1, measured by the aforementioned metrics.

Configuration	Database	Kidney DSC	Tumor DSC	Kidney IoU	Tumor IoU
3D full resolution	KiTS 19'	96.2%	84.3%	92.7%	74.7%
3D full resolution	KiTS 23'	94.3%	79.5%	90.2%	70.8%
3D low resolution	KiTS 23'	92.2%	79.7%	87.5%	71.1%
3D cascade	KiTS 23'	93.6%	76.2%	89.1%	67.2%

Table 5.1: Segmentation results on different databases, using different configurations

In order to benchmark our approach, we can compare to the results obtained in the Kidney and Kidney Tumor Segmentation Challenge from 2023. We can see the top 10 results in Table 5.2. To work on the same conditions, we will consider our results on the KiTS23' database. It is clear that our approach achieved better results on the tumor segmentations, with over a 4% increase in the Dice score. They haven't provided the accuracy for kidney segmentation, but it is the tumor segmentation that matters more, as it is the malignancy we are trying to get rid of. Additionally, our model trained on KiTS19' achieved even better results that those. This shouldn't be considered straightly better, as we haven't tested on the same cohort. It was our goal to test all the methods on the KiTS23' test set, but it isn't publicly available, and haven't received any notice from the organizers.

Place	Team	Dice Score	Tumor Dice Score
1	Andriy Myronenko et al. [110]	0.835	0.758
2	Kwang-Hyun Uhm [111]	0.820	0.738
3	Yasmeen George [112]	0.819	0.713
4	Shuolin Liu [113]	0.805	0.697
5	George Stoica et al. [114]	0.807	0.713
6	Lifei Qian et al. [92]	0.801	0.687
7	Ziyan Huang et al.	0.794	0.686
8	Zohaib Salahuddin et al. [115]	0.795	0.690
9	Cancan Chen [89]	0.799	0.691
10	Joffrey Michaud [116]	0.790	0.670

Table 5.2: Top 10 results in the KiTS23' Challenge.

We can show segmentation predictions on the cases from KiTS19', which was the configuration that had the best results. We won't show all of the predictions, just some of them that illustrate the possible problems encountered, and cases in which it performs perfectly. The segmentation metrics for these cases are displayed in Table 5.3.

Image	**Kidney DSC**	**Tumor DSC**	**Kidney IoU**	**Tumor IoU**
KiTS-00002	97.5%	92.2%	95.1%	85.6%
KiTS-00042	93.8%	69.2%	88.4%	52.8%
KiTS-00050	97.9%	82.8%	95.9%	70.7%
KiTS-00120	96.8%	47.0%	93.9%	30.8%
KiTS-00150	98.0%	91.7%	96.1%	84.6%
KiTS-00172	94.6%	96.7%	89.8%	93.6%
KiTS-00199	95.4%	93.1%	91.1%	87.1%
KiTS-00207	97.6%	75.9%	95.4%	61.2%

Table 5.3: Segmentation metrics of the 3D full resolution configuration predictions trained on KiTS19' on some of the cases from the validation set.

For case KiTS-00002, we got a 97.5% Dice score for kidney segmentation and 92.2% for the tumor. We can see the results in Fig. 5.1, and how the network is able to distinguish the cyst at the top of the left kidney from a tumor.

For case KiTS-00042, we got a 93.8% Dice score for kidney segmentation and 69.2% for the tumor. We can see the results in Fig. 5.2. The segmentation fails as the tumor is extensive, even bigger than the kidneys. This case would fall out of the scope of this project, as a tumor this big wouldn't be treated via IGTA.

For case KiTS-00120, we got a 96.8% Dice score for kidney segmentation and 47.0% for the tumor(s). We can see the results in Fig. 5.3. Opposite to the previous case, this tumor

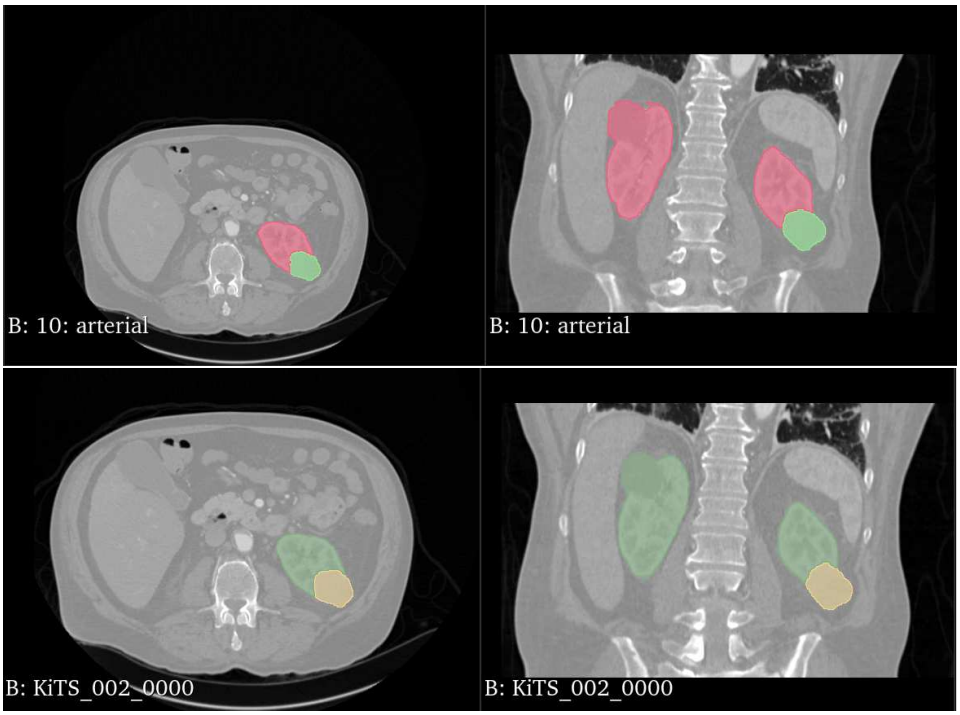

Figure 5.1: Comparison of patient KiTS-00002 ground-truth segmentation (up, kidneys in red and tumor in green) and prediction (down, kidneys in green and tumor in yellow) by 3D full resolution network trained on KiTS19', displayed in 3D Slicer.

is extremely small. The network is not able to properly define the tumor boundaries and overestimates them.

For case KiTS-00150, we got a 98.0% Dice score for kidney segmentation and 91.7% for the tumor(s). We can see the results in Fig. 5.4. Despite the problem with the intensity rescaling, the network performed well, except for some inner space in the middle of the kidneys that shouldn't be segmented.

For case KiTS-00172, we got a 94.6% Dice score for kidney segmentation and 96.7% for the tumor(s). We can see the results in Fig. 5.5. In this case we are also dealing with a patient with a disproportionate tumor size, although it works excellent.

For case KiTS-00199, we got a 95.45% Dice score for kidney segmentation and 93.1% for the tumor(s). We can see the results in Fig. 5.6. Despite the inadequate intensity rescaling, the network performs fairly well. As in previous cases, is fails to exclude small portions of the renal pelvis (non-segmented spaces in the middle of the kidney).

For case KiTS-00207, we got a 97.6% Dice score for kidney segmentation and 75.9% for the tumor(s). We can see the results in Fig. 5.7. In this case, the ground-truth segmentation is very blocky, caused by the low axial resolution. Even after interpolation, this is not solved,

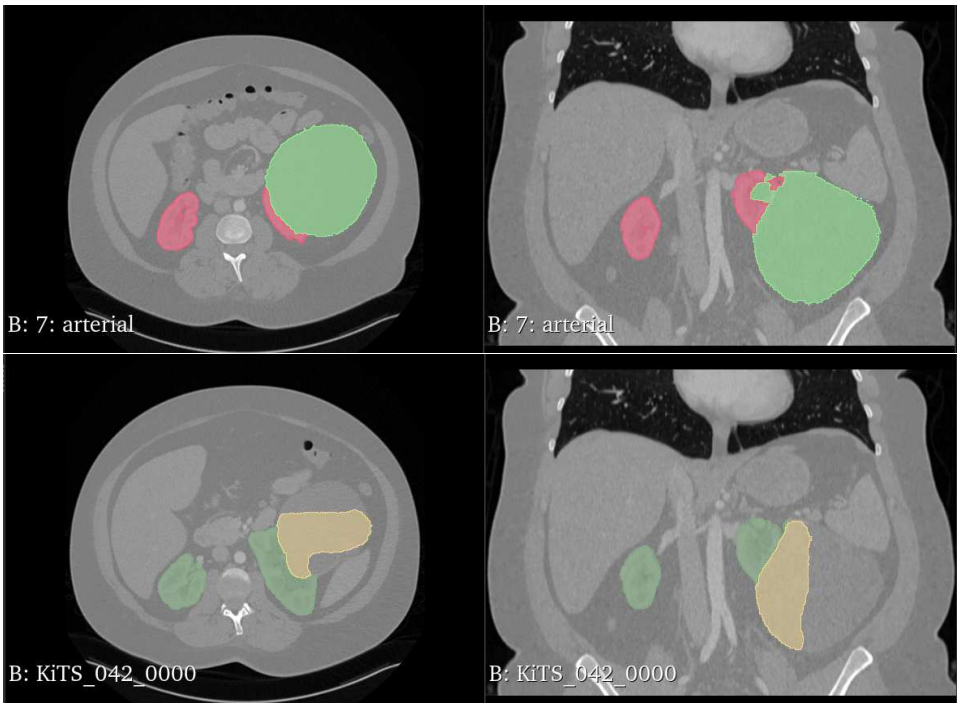

Figure 5.2: Comparison of patient KiTS-00042 ground-truth segmentation (up, kidneys in red and tumor in green) and prediction (down, kidneys in green and tumor in yellow) by 3D full resolution network trained on KiTS19', displayed in 3D Slicer.

so error is induced. More discrepancy in the metrics is added by segmentation of part of the glenohumeral joint (shoulder).

We also show some of the segmentations predicted by the 3D full resolution nnU-Net trained on KiTS23'. It is the configuration that rendered better results while training on the KiTS23' database.

For the case KiTS-00042 in Fig. 5.8, we obtained a 93.1% Dice score for the kidneys, 84.3% for tumor(s), and 0.0% for cysts (there were no cysts in the ground-truth). We can compare how both approaches performed in this case, and it turns out that the segmentation of the tumor is much better in this case. The problem arises in the kidney segmentation, as this approach (trained on KiTS23') determines that the center of the right kidney is a cyst, which shouldn't be labeled as such.

For the case KiTS-00117 in Fig. 5.9, we obtained a 75.5% Dice score for the kidneys, 72.7% for tumor(s), and 0.0% for cysts (the existing cysts weren't found). It is a difficult case containing two tumors and 3 cysts. Still, the network wasn't able to understand the shape of the kidneys, cutting their extension and wrongly labeling the renal pelvis. It also

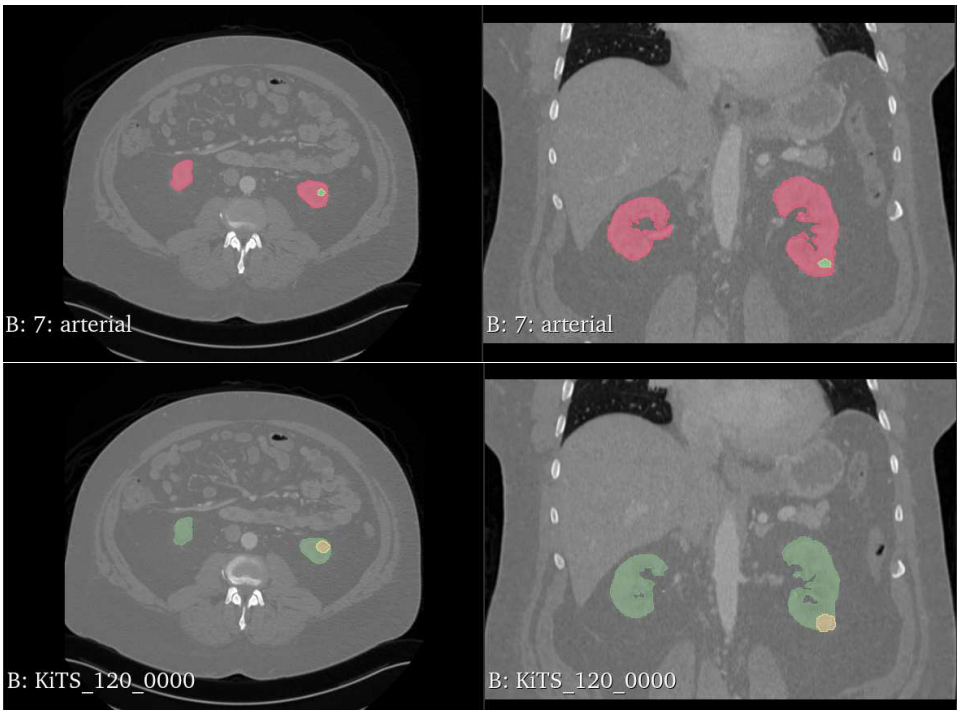

Figure 5.3: Comparison of patient KiTS-00120 ground-truth segmentation (up, kidneys in red and tumor in green) and prediction (down, kidneys in green and tumor in yellow) by 3D full resolution network trained on KiTS19', displayed in 3D Slicer.

cut the found tumors. These errors might be related to intensity rescaling problems, as the shape is easily perceived.

For the case KiTS-00141 in Fig. 5.10, we obtained a 98.3% Dice score for the kidneys, 89.5% for tumor(s), and 96.1% for cysts. The network performs well in this case, excluding the renal pelvis, and recognizing everything with good accuracy.

The inclusion of cysts in the labels caused a decreased overall performance in segmentation. This might be caused by the difficulty to differentiate cysts from tumors.

We also tested the performance of our best model, the 3D full resolution architecture trained on KiTS19', on the Johns Hopkins database. This database doesn't include ground-truth segmentations, so the evaluation is qualitatively done by visual inspection. The images were in the same format as the database on which the model was trained, although JHU includes a variety of non-contrast and contrast-enhanced CT and MRI scans, which are disclosed in Table 5.4. The GPU time needed for running the prediction on the 230 scans was approximately 23 hours and 30 minutes. This would give us an average of approxiamtely 6 minutes per image prediction.

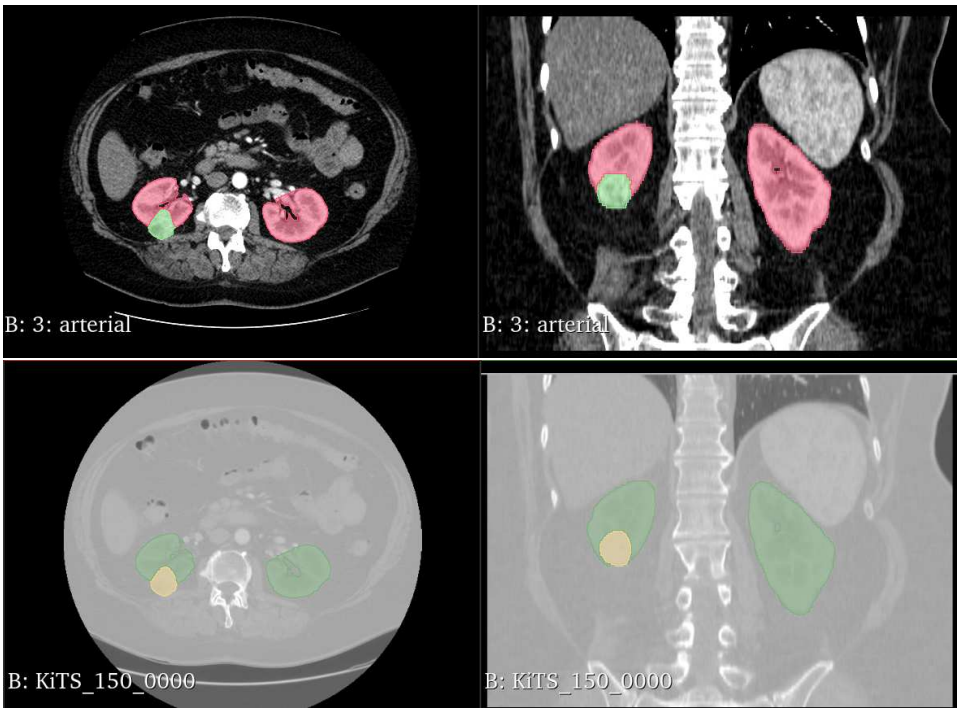

Figure 5.4: Comparison of patient KiTS-00150 ground-truth segmentation (up, kidneys in red and tumor in green) and prediction (down, kidneys in green and tumor in yellow) by 3D full resolution network trained on KiTS19', displayed in 3D Slicer.

We produced the manual segmentation of some of the cases, just to be able to compute some metrics to evaluate the precision of the model. I created these ground-truth segmentations by manually labeling on ITK Snap and saved them. It has been created from the knowledge acquired by working on these databases throughout a year. However, it is still not comparable to the ground-truth segmentations produced by attending physicians.

The prediction on case JHU_007 seems to properly adjust to the kidney shape, as seen in Fig. 5.11. The trained model wasn't able to find a tumor in the image, which definitely existed, but was difficult to find by visual inspection in a plain CT scan. Visualization of this image required adjusting window width and level in 3D Slicer to differentiate tissues.

The prediction on case JHU_014 can be found in Fig. 5.12. It seems to work fairly well, as it is able to exclude the renal pelvis, and it does find a tumor inside the kidney.

The prediction on case JHU_015 apparently finds the kidney with good accuracy, as per Fig. 5.13. Regardless, the tumor shape and location seem strange. It is also important to note that it is the same patient as in the previous image, so such a difference in tumor location might not be true.

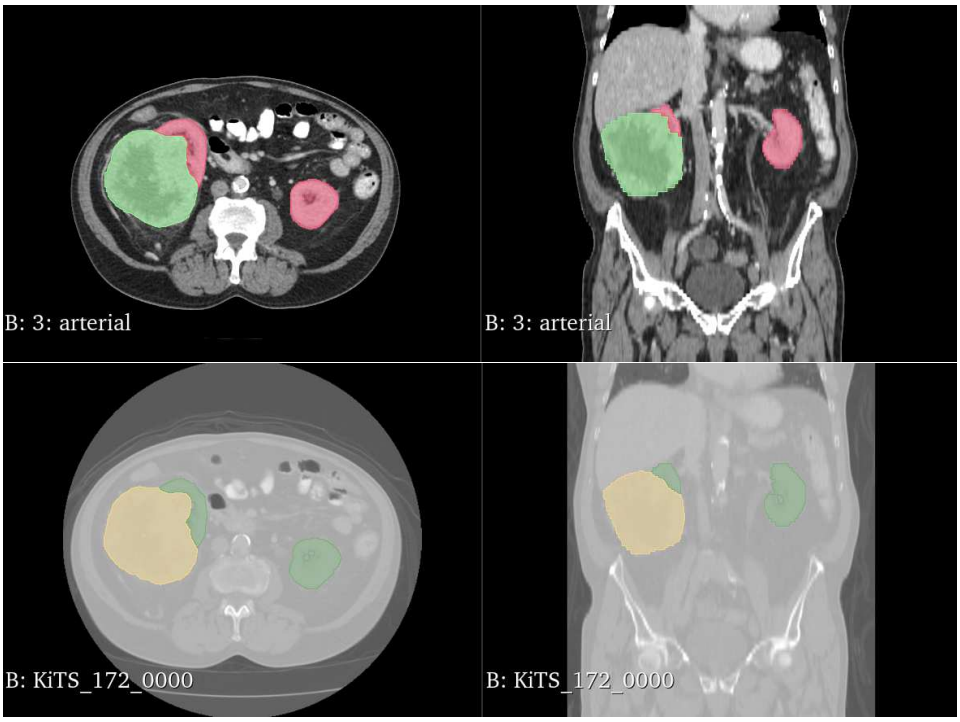

Figure 5.5: Comparison of patient KiTS-00172 ground-truth segmentation (up, kidneys in red and tumor in green) and prediction (down, kidneys in green and tumor in yellow) by 3D full resolution network trained on KiTS19', displayed in 3D Slicer.

For case JHU_016, the prediction in Fig. 5.14 looks like it was able to find the kidney and tumor properly. The problem is it segmented part of the ureter, which shouldn't be labeled. This image also corresponds to the same patient as before, and there is a big difference with case JHU_015, and much resemblance to JHU_014.

For case JHU_018, the model is able to label the kidney and a tumor very well. It was a difficult case given that it is a simple CT scan (on which the network is not trained) and the noise in the image. We can see it in Fig. 5.15.

The kidney is finely delineated in case JHU_021, as seen in Fig. 5.16. The model correctly excludes the renal pelvis from the segmentation, although the tumor seems to be a little bigger than predicted.

As seen in Fig. 5.17, our model doesn't work for segmenting MRI images like case JHU_022. It makes sense as it was trained only on contrast CTs, and imaging modalities are very different.

In case JHU_055, our model is able to perfectly capture the kidney and a tumor, despite the bad image quality. We can see how the image is blurry in the coronal plane and the wrong intensity rescaling in Fig. 5.18.

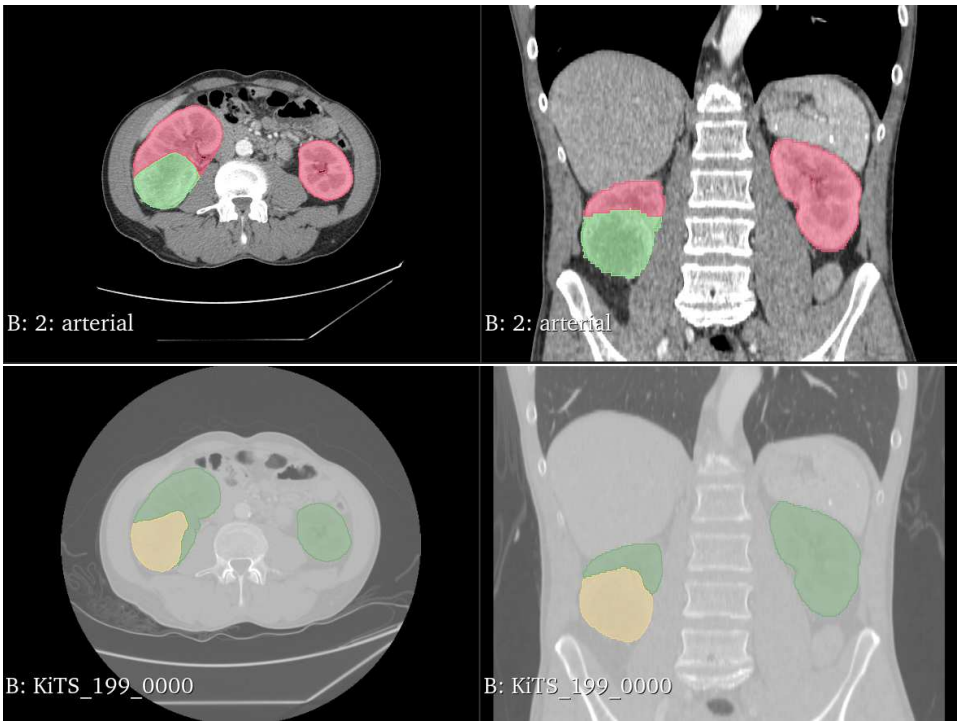

Figure 5.6: Comparison of patient KiTS-00199 ground-truth segmentation (up, kidneys in red and tumor in green) and prediction (down, kidneys in green and tumor in yellow) by 3D full resolution network trained on KiTS19', displayed in 3D Slicer.

Our model performs well on case JHU_068, which was evaluated because of the herniation on the right side of the patient. It helps to conclude that strange body morphologies don't affect much in the segmentation prediction, as seen in Fig. 5.19.

We can compare the prediction on JHU_073 with our ground-truth. We found a 98.4% DSC on the kidney, and 93.9% on the tumor segmentations.

From JHU_081 prediction, we see that our model doesn't work properly on simple CT scans, as no segmentation was found in this case. As we can see in Fig. 5.21 the kidneys are visible, although the model can't find them.

We used case JHU_137 for testing on a distorted image, as the file contains two instances of the CT scan, and should be properly separated. As we can see in Fig. 5.22, the model is able to perfectly find the kidneys in one of the images, and some parts of it on the second one. Localization on the top instance doesn't work well, but at least there are no false positives.

The prediction of JHU_165 is good, finding the tumor and the right kidney without problems, but cutting the left kidney. It is interesting that the model is able to make such a good prediction of the right kidney, which is somewhat distorted because of a herniation on

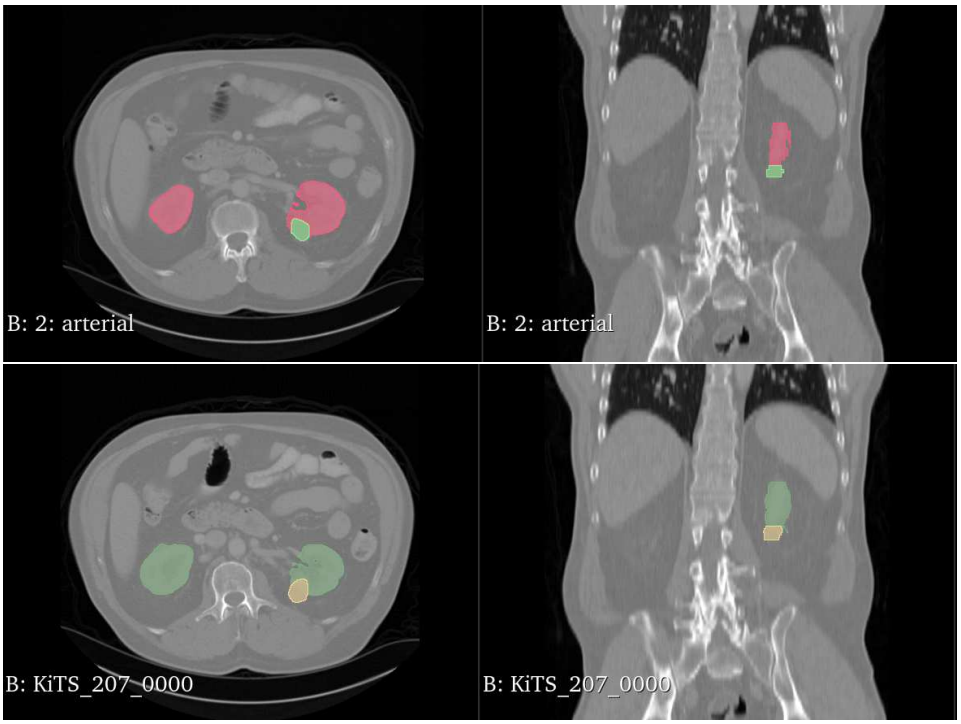

Figure 5.7: Comparison of patient KiTS-00207 ground-truth segmentation (up, kidneys in red and tumor in green) and prediction (down, kidneys in green and tumor in yellow) by 3D full resolution network trained on KiTS19', displayed in 3D Slicer.

the right side of the patient, and has problems with the left kidney. We can see that in Fig. 5.23.

Testing again on another MRI image has the same results as before. We can see the T2-weighted image of case JHU_179 in Fig. 5.24, which has no predicted segmentation.

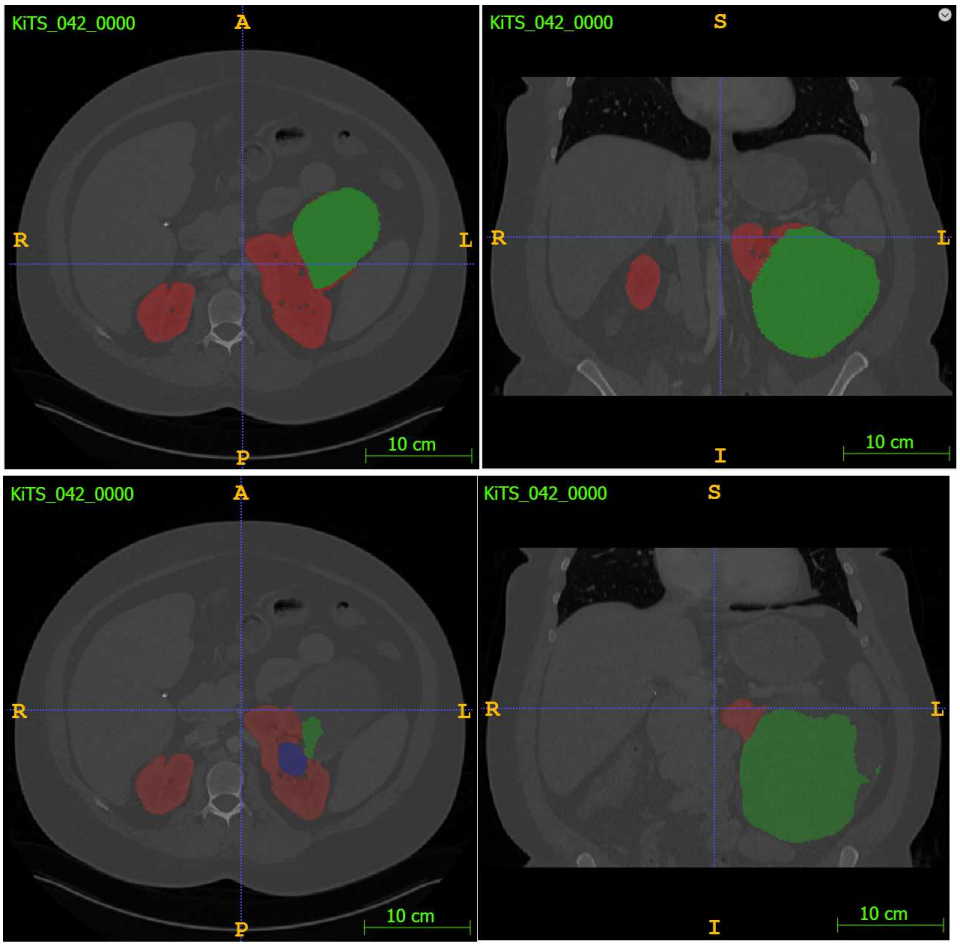

Figure 5.8: Comparison of patient KiTS-00042 ground-truth segmentation (up) and prediction (down) by 3D full resolution network trained on KiTS23', displayed in 3D Slicer (kidneys in red, tumor in green and cysts in blue).

Case name	Image modality
JHU_007	CT
JHU_014	Contrast CT
JHU_015	Contrast CT
JHU_016	Contrast CT
JHU_018	CT
JHU_021	Contrast CT
JHU_022	T1-weighted MRI
JHU_055	CT
JHU_068	Contrast CT
JHU_081	CT
JHU_137	CT
JHU_165	Contrast CT
JHU_179	T2-weighted MRI

Table 5.4: Modalities of the cases from JHU database used evaluated for prediction.

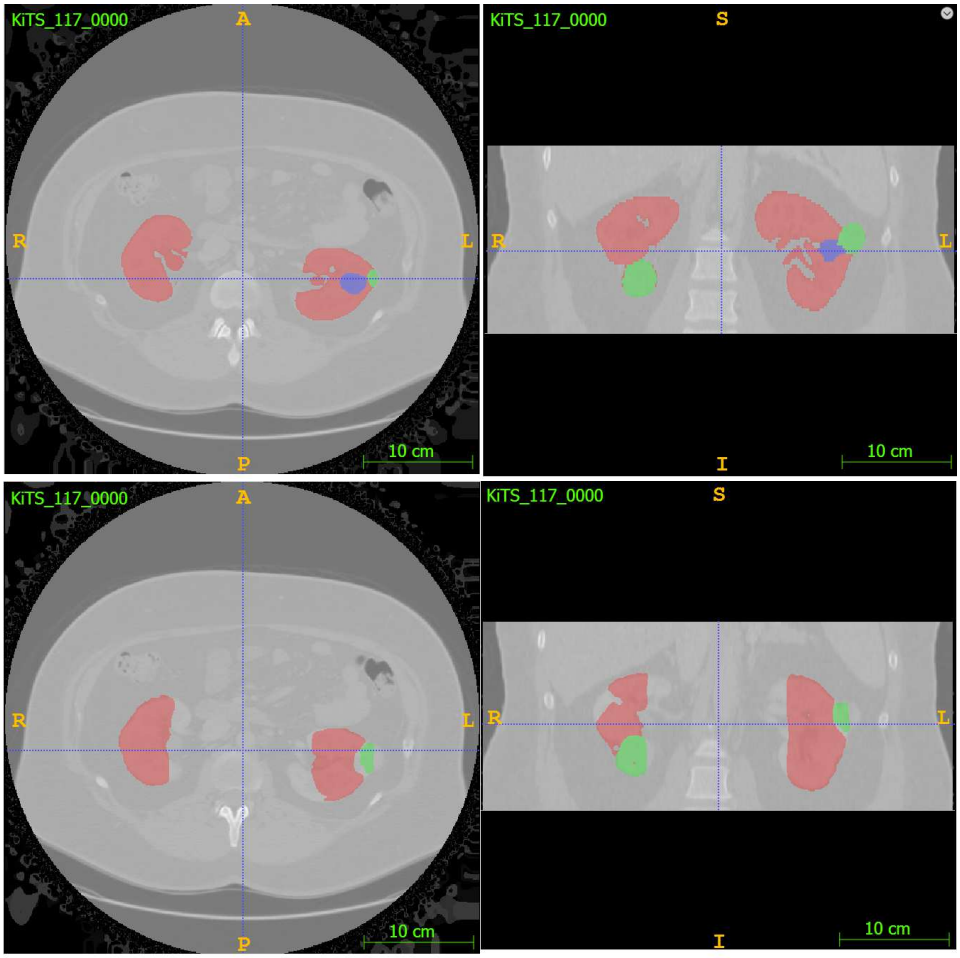

Figure 5.9: Comparison of patient KiTS-00117 ground-truth segmentation (up) and prediction (down) by 3D full resolution network trained on KiTS23', displayed in ITK Snap, (kidneys in red, tumor in green, and cysts in blue).

Image	Kidney DSC	Tumor DSC	Kidney IoU	Tumor IoU
JHU_014	98.9%	100.0%	97.9%	100.0%
JHU_068	99.5%	89.3%	98.9%	80.6%
JHU_073	98.4%	93.9%	96.9%	88.6%

Table 5.5: Segmentation metrics of the 3D full resolution configuration predictions trained on KiTS19' on the JHU database with manual segmentations.

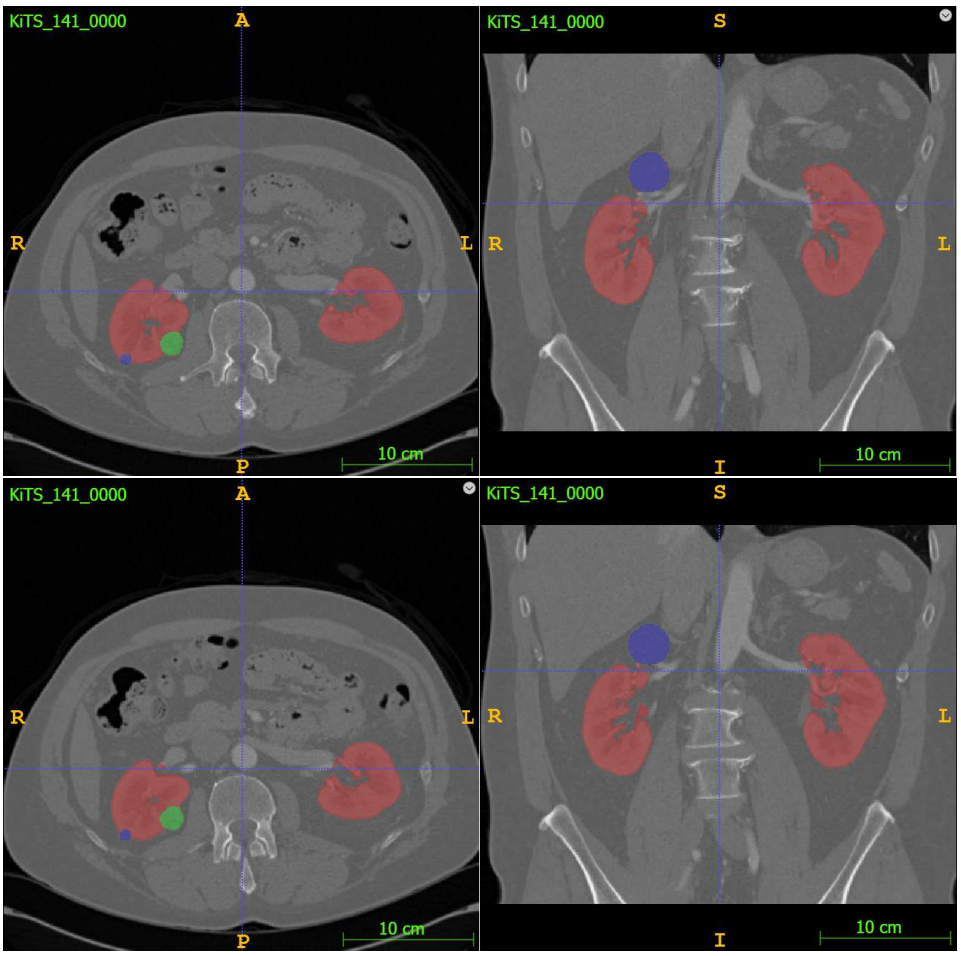

Figure 5.10: Comparison of patient 141 ground-truth segmentation (up) and prediction (down) by 3D full resolution network trained on KiTS23', displayed in 3D Slicer(kidneys in red, tumor in green and cysts in blue).

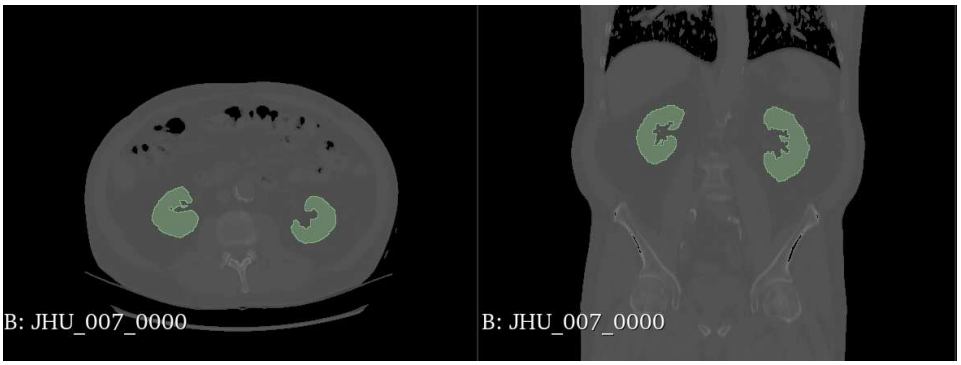

Figure 5.11: Segmentation prediction on JHU_007 by nnU-Net 3D full resolution model trained on KiTS19', visualized in 3D Slicer.

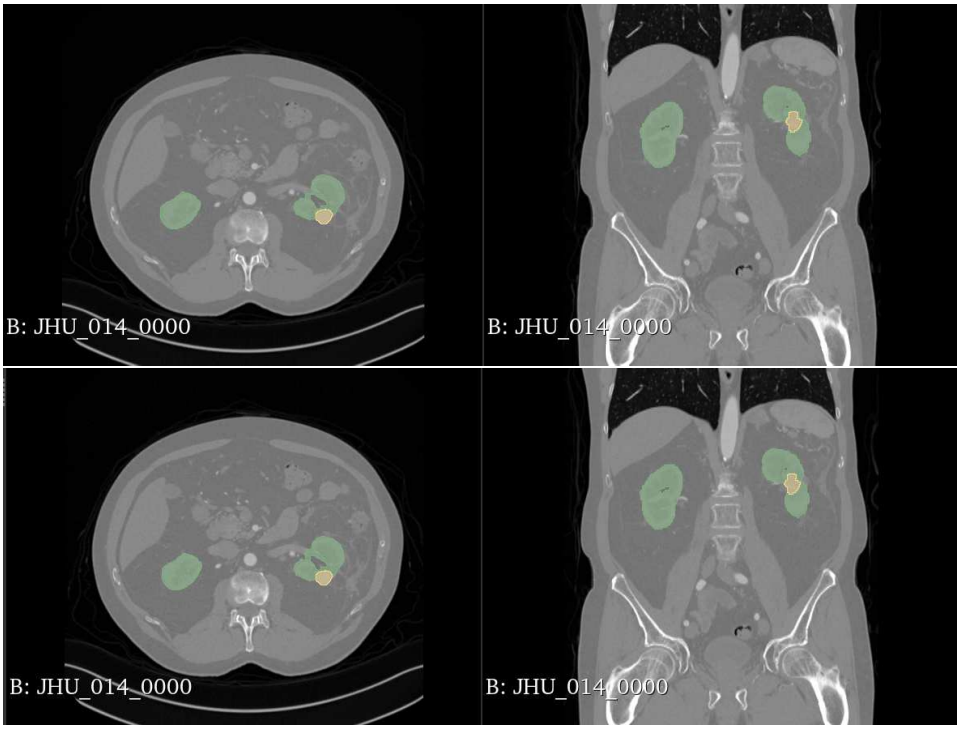

Figure 5.12: Comparison of patient JHU_014 ground-truth segmentation (up) and segmentation prediction by nnU-Net 3D full resolution model trained on KiTS19' (down), visualized in 3D Slicer.

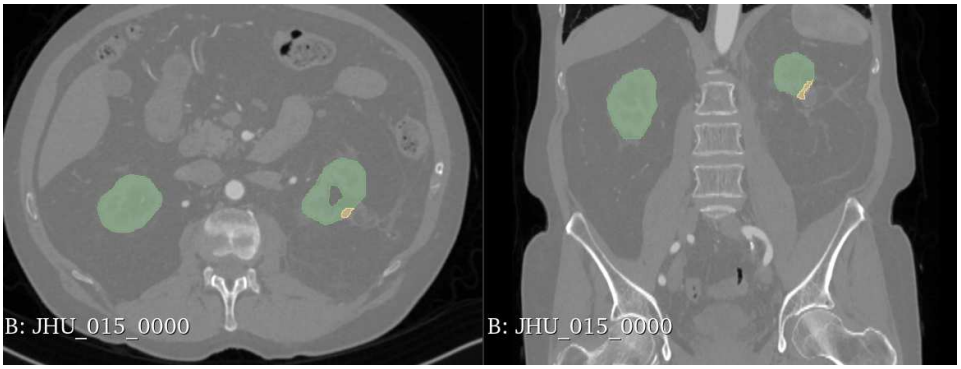

Figure 5.13: Segmentation prediction on JHU_015 by nnU-Net 3D full resolution model trained on KiTS19', visualized in 3D Slicer.

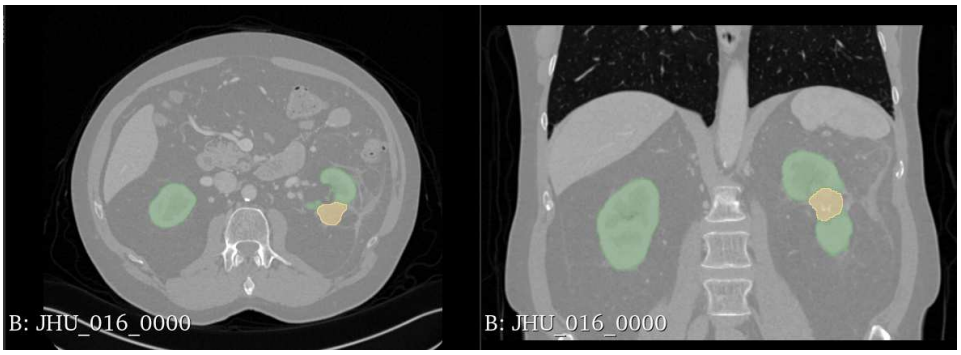

Figure 5.14: Segmentation prediction on JHU_016 by nnU-Net 3D full resolution model trained on KiTS19', visualized in 3D Slicer.

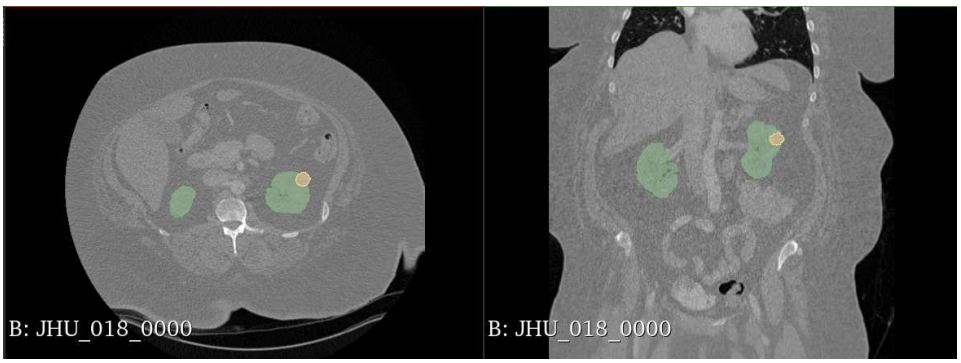

Figure 5.15: Segmentation prediction on JHU_018 by nnU-Net 3D full resolution model trained on KiTS19', visualized in 3D Slicer.

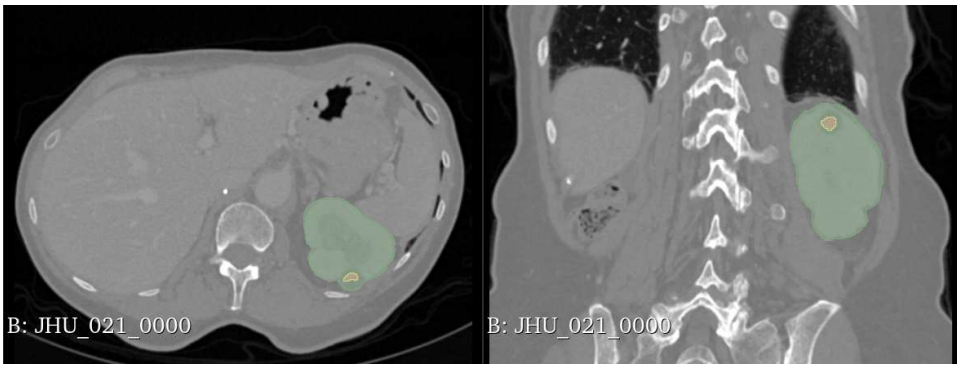

Figure 5.16: Segmentation prediction on JHU_021 by nnU-Net 3D full resolution model trained on KiTS19', visualized in 3D Slicer.

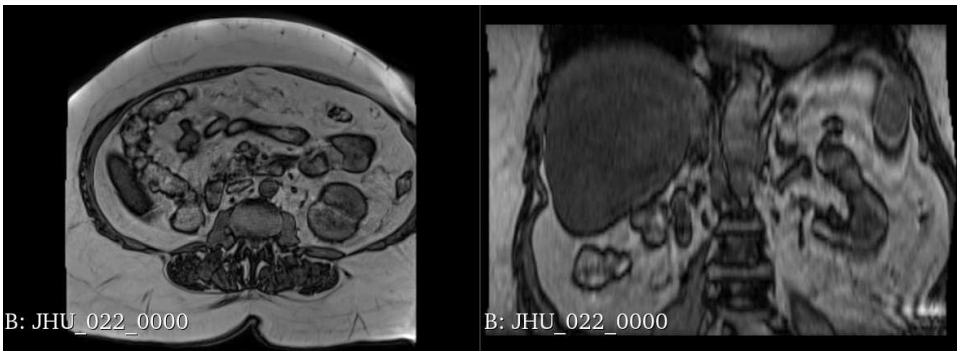

Figure 5.17: Segmentation prediction on JHU_022 by nnU-Net 3D full resolution model trained on KiTS19', visualized in 3D Slicer.

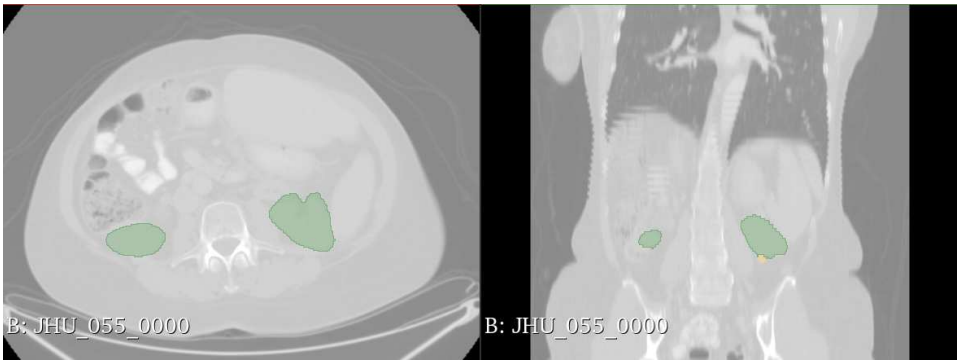

Figure 5.18: Segmentation prediction on JHU_055 by nnU-Net 3D full resolution model trained on KiTS19', visualized in 3D Slicer.

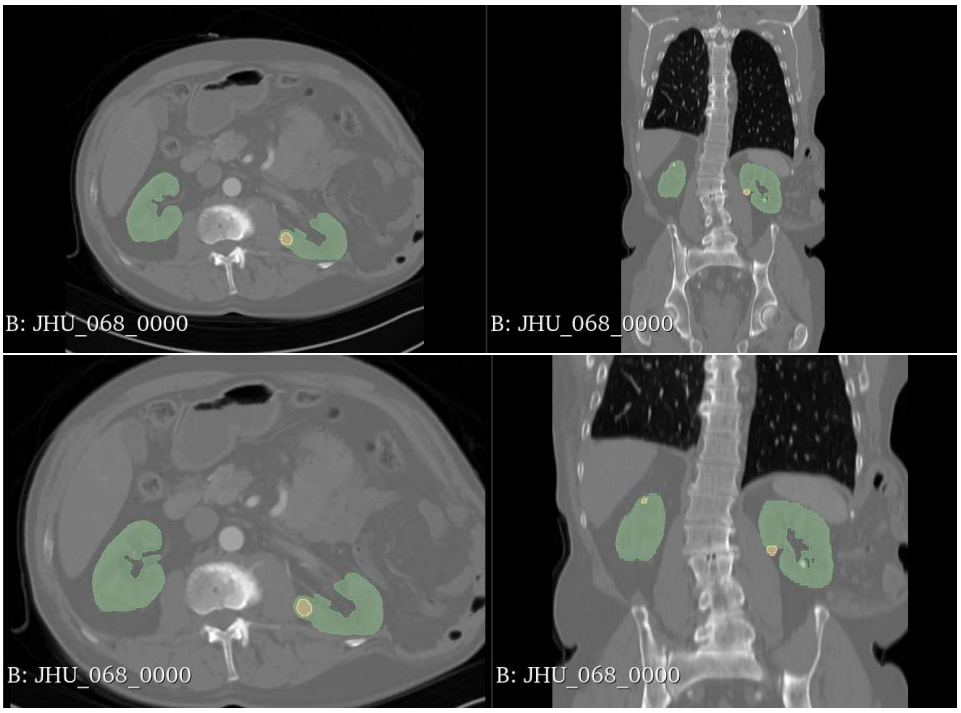

Figure 5.19: Comparison of patient JHU_068 ground-truth segmentation (up) and segmentation prediction by nnU-Net 3D full resolution model trained on KiTS19' (down), visualized in 3D Slicer.

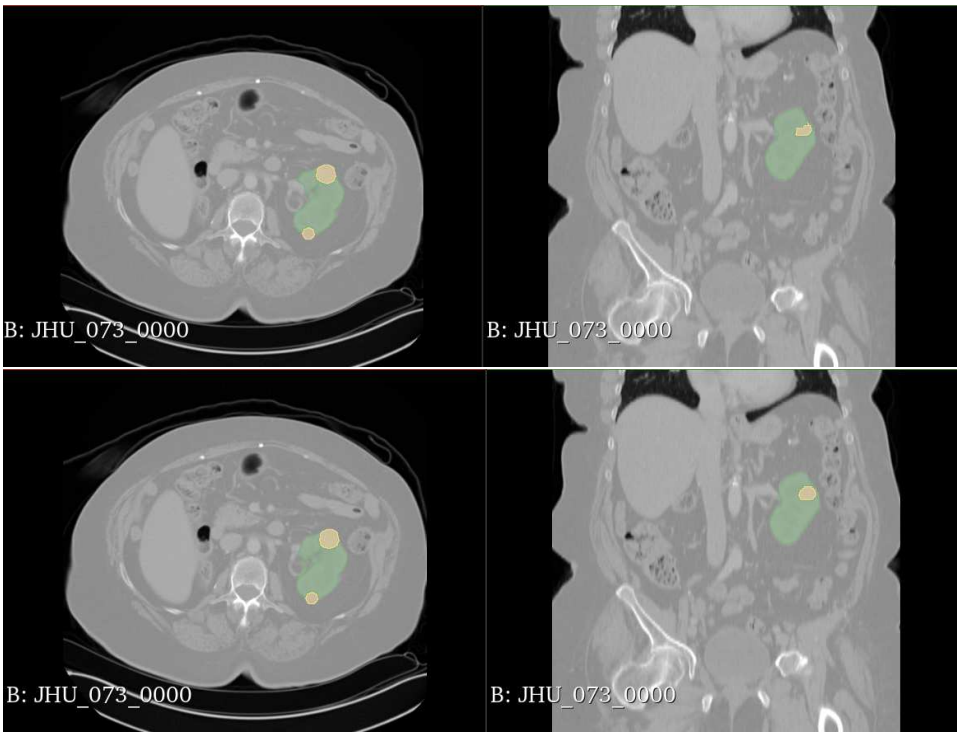

Figure 5.20: Comparison of patient JHU_073 ground-truth segmentation (up) and segmentation prediction by nnU-Net 3D full resolution model trained on KiTS19' (down), visualized in 3D Slicer.

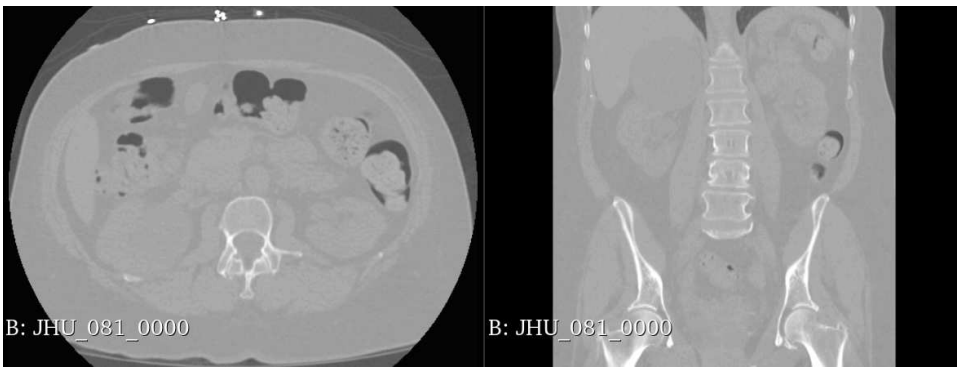

Figure 5.21: Segmentation prediction on JHU_081 by nnU-Net 3D full resolution model trained on KiTS19', visualized in 3D Slicer.

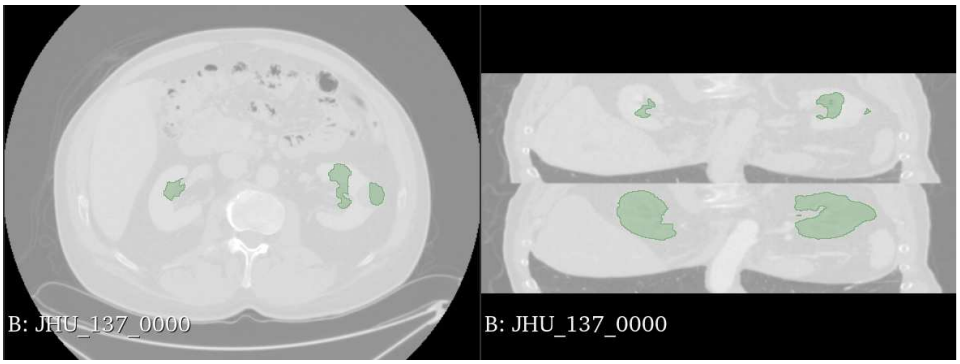

Figure 5.22: Segmentation prediction on JHU_137 by nnU-Net 3D full resolution model trained on KiTS19', visualized in 3D Slicer.

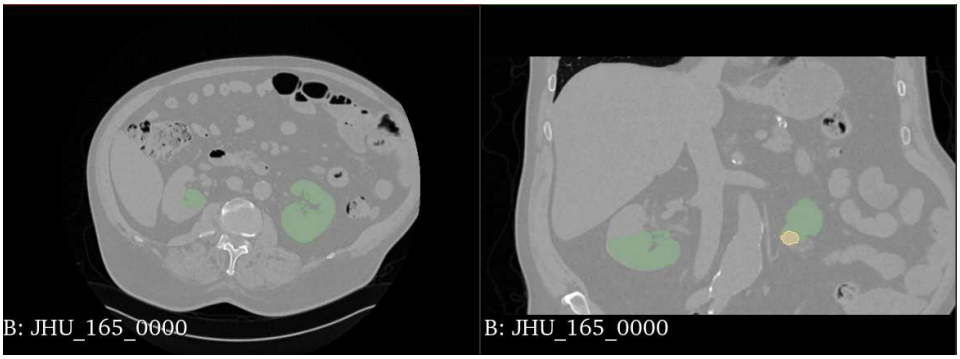

Figure 5.23: Segmentation prediction on JHU_165 by nnU-Net 3D full resolution model trained on KiTS19', visualized in 3D Slicer.

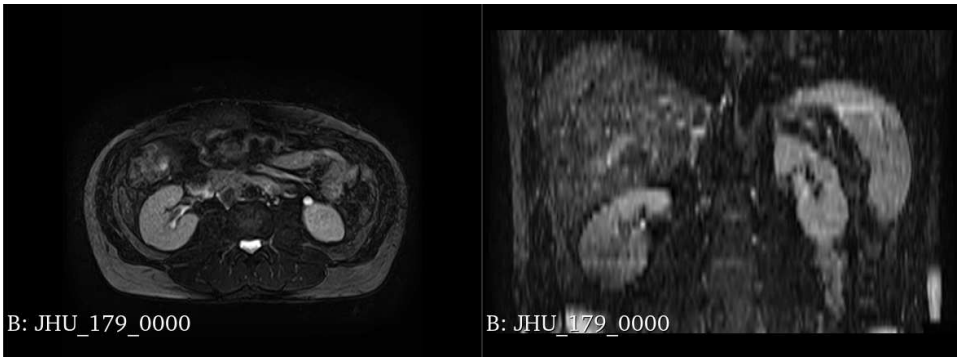

Figure 5.24: Segmentation prediction on JHU_179 by nnU-Net 3D full resolution model trained on KiTS19', visualized in 3D Slicer.

Chapter 6

Conclusions

After creating different models, training, and testing on different databases, we can conclude that the deep learning-assistance for segmentation of kidneys and tumors in renal tumor image-guided thermal ablation is feasible, but still needs improvement before its potential use in a clinical setting. On the one hand, achieving over 92% accuracy (measured by Dice coefficient) for kidney segmentation is significant, and may be enough for use in clinical cases, although it might be difficult to improve in this regard. As was noted in [108], the segmentations from different medicine students had a 92% DSC. Therefore, we can consider anything above that threshold to be clinically significant, as that is already the variability between two ground-truths. On the other hand, the accuracy for tumor and cyst segmentation isn't good enough and should be improved, given that the goal is to use this for tumor treatment.

The first step that should be taken to improve this would be to curate a proper database, with a higher number of cases, including different modalities. As we saw from Johns Hopkins database, staging and disease assessment are not only done on contrast-enhanced CT scans. Different cases and patients may require information from different modalities to properly assess the case at hand. This database would also need segmentations generated by attending physicians to ensure we are using the best possible data to train our model. It would be important to only include cases from patient who have previously undergone this same procedure, image-guided thermal ablation, to make sure we are creating a tool that is useful for our ultimate goal.

In the model's regard, we have used the same algorithms that placed at the top in the Kidney and Kidney Tumor Segmentation Challenge in its last edition. We even achieve better

segmentation on the tumors with the 3D full-resolution models. Still, there might be better options to perform this task, which might include the combination of attention modules, transformers, or generative approaches, which have also rendered good results in such tasks.

Chapter 7

Future Work

All of the work done in this project sheds light on our goal, but it is not sufficient. Firstly, we need to improve our accuracy to be able to introduce our approach in a clinical setting. In order to improve our performance, there are several paths we could take to do so. The first step that should be evaluated and potentially changed is our preprocessing. Firstly, instead of resizing all of the images into a $512 \times 512 \times 256$ size, there might be a different number of axial slices that would cause less error in interpolation. Additionally, we could consider cropping the input images, and focusing better on the abdominal region in those images that include a wider field of view. Lastly, our intensity rescaling has proven to be somewhat faulty and result in some images in which the intensity scales allow for little contrast between normally differentiable tissues.

Secondly, we should create an improved database on which to train and benchmark different approaches. If our goal is to only use it for IGTA patients, our training cases should be patients that have been, or would be treated by thermal ablation. Additionally, we found from Johns Hopkins archive, that clinicians not inly use contrast-enhanced CTs in their pre-operative stuides, but also include MRIs and non-enhanced CTs. In order to completely integrate our approach in a potential clinical pipeline, we would need to include, and potentially con¡mbine, the information offered by each of the imaging modalities.

Moreover, we could create different architectures, or additional modules, that might be able to improve our model's performance. We truly need to improve the accuracy of our method for its integration in the surgery room. The error generated by the inclusion of cysts in the database might also be addressed in this way, as we need to be able to differentiate between them. If we are able to find an architecture which depends on a lower number of

parameters, and is able to run inference in a shorter time it would be a bonus point, as the we need the fastest response in a surgical environment.

Lastly, our next step in this project would be performing the registration of pre-operative scans with the intra- or post-operative scans. The goal of this is to understand the biomechanical deformation underwent throughout the procedure, as well as to give the physicians a grasp of the ablation extent and success. It is of utmost importance to be able to assess the extent of the procedure, and whether the whole tumor has been successfully ablated, to avoid recurrence.

References

.....

[1] C. J. Weight *et al.*, "Nephrectomy Induced Chronic Renal Insufficiency is Associated With Increased Risk of Cardiovascular Death and Death From Any Cause in Patients With Localized cT1b Renal Masses," EN, *Journal of Urology*, Apr. 2010, Publisher: Wolters KluwerPhiladelphia, PA. DOI: 10.1016/j.juro.2009.12.030. [Online]. Available: https://www.auajournals.org/doi/10.1016/j.juro.2009.12.030 (visited on 04/10/2025).

[2] M. Regier and F. Chun, "Thermal Ablation of Renal Tumors: Indications, Techniques and Results," *Deutsches Ärzteblatt International*, vol. 112, no. 24, pp. 412–418, Jun. 2015. DOI: 10.3238/arztebl.2015.0412. [Online]. Available: https://www.ncbi.nlm.nih.gov/pmc/articles/PMC4500057/ (visited on 04/10/2025).

[3] *Cancer*, en. [Online]. Available: https://www.who.int/health-topics/cancer#tab=tab_1 (visited on 02/04/2025).

[4] *Cancer Facts & Figures 2024*, en. [Online]. Available: https://www.cancer.org/research/cancer-facts-statistics/all-cancer-facts-figures/2024-cancer-facts-figures.html (visited on 02/07/2025).

[5] *Cancer Facts & Figures 2025*, en. [Online]. Available: https://www.cancer.org/research/cancer-facts-statistics/all-cancer-facts-figures/2025-cancer-facts-figures.html (visited on 02/06/2025).

[6] B. D. Preston, T. M. Albertson, and A. J. Herr, "DNA Replication Fidelity and Cancer," *Seminars in cancer biology*, vol. 20, no. 5, pp. 281–293, Oct. 2010. DOI: 10.1016/j.semcancer.2010.10.009. [Online]. Available: https://www.ncbi.nlm.nih.gov/pmc/articles/PMC2993855/ (visited on 03/16/2025).

[7] *Antioxidants and Cancer Prevention - NCI*, en, cgvArticle, Archive Location: nciglobal,ncienterprise, Jan. 2014. [Online]. Available: https://www.cancer.gov/about-cancer/causes-prevention/risk/diet/antioxidants-fact-sheet (visited on 03/16/2025).

[8] M. F. Kane *et al.*, "Methylation of the hMLH1 Promoter Correlates with Lack of Expression of hMLH1 in Sporadic Colon Tumors and Mismatch Repair-defective Human Tumor Cell Lines1," *Cancer Research*, vol. 57, no. 5, pp. 808–811, Mar. 1997.

[9] B. Alberts *et al.*, "The Molecular Basis of Cancer-Cell Behavior," en, in Garland Science, 2002. [Online]. Available: https://www.ncbi.nlm.nih.gov/books/NBK26902/ (visited on 03/16/2025).

[10] R. D. Rosen and A. Sapra, "TNM Classification," eng, in *StatPearls*, Treasure Island (FL): StatPearls Publishing, 2023. [Online]. Available: http://www.ncbi.nlm.nih.gov/books/NBK553187/ (visited on 06/05/2023).

[11] *Cancer Staging - NCI*, en, cgvArticle, Archive Location: nciglobal,ncienterprise, Mar. 2015. [Online]. Available: https://www.cancer.gov/about-cancer/diagnosis-staging/staging (visited on 03/17/2025).

[12] *Carcinoma: Types, Treatment & What it Is*. [Online]. Available: https://my.clevelandclinic.org/health/diseases/23180-carcinoma (visited on 03/28/2025).

[13] *Epithelium: What It Is, Function & Types*, en. [Online]. Available: https://my.clevelandclinic.org/health/articles/22062-epithelium (visited on 03/28/2025).

[14] B. I. Rini, S. C. Campbell, and B. Escudier, "Renal cell carcinoma," en, [Online]. Available: https://www.thelancet.com/journals/lancet/article/PIIS0140-6736(09)60229-4/fulltext (visited on 03/17/2025).

[15] J. J. Hsieh *et al.*, "Renal cell carcinoma," en, *Nature Reviews Disease Primers*, vol. 3, no. 1, pp. 1–19, Mar. 2017, Publisher: Nature Publishing Group. DOI: 10.1038/nrdp.2017.9. [Online]. Available: https://www.nature.com/articles/nrdp20179 (visited on 03/17/2025).

[16] *Kidney cancer statistics*, en-GB. [Online]. Available: https://www.wcrf.org/preventing-cancer/cancer-statistics/kidney-cancer-statistics/ (visited on 02/13/2025).

[17] U. Capitanio *et al.*, "Epidemiology of Renal Cell Carcinoma," *European Urology*, vol. 75, no. 1, pp. 74–84, Jan. 2019. DOI: 10.1016/j.eururo.2018.08.036. [Online]. Available: https://www.sciencedirect.com/science/article/pii/S030228381830633X (visited on 02/13/2025).

[18] *Cruciferous Vegetables Consumption and Risk of Renal Cell Carcinoma: A Meta-Analysis: Nutrition and Cancer: Vol 65, No 5*. [Online]. Available: https://www.tandfonline.com/doi/abs/10.1080/01635581.2013.795980?casa_token=ieIALVyJXFUAAAAA:Dtjym-xyleDilqg8ZLnKK6JAZbEV25yVAlkpjW85qHDgusdR5JhYkC7iE4QwZToA7 (visited on 02/13/2025).

[19] G. Behrens and M. F. Leitzmann, "The association between physical activity and renal cancer: Systematic review and meta-analysis," en, *British Journal of Cancer*, vol. 108, no. 4, pp. 798–811, Mar. 2013, Publisher: Nature Publishing Group. DOI: 10.1038/bjc.2013.37. [Online]. Available: https://www.nature.com/articles/bjc201337 (visited on 02/13/2025).

[20] J. Q. Lew *et al.*, "Alcohol consumption and risk of renal cell cancer: The NIH-AARP diet and health study," en, *British Journal of Cancer*, vol. 104, no. 3, pp. 537–541, Feb. 2011, Publisher: Nature Publishing Group. DOI: 10.1038/sj.bjc.6606089. [Online]. Available: https://www.nature.com/articles/6606089 (visited on 02/13/2025).

[21] R. Jay *et al.*, "Alcohol consumption and the risk of renal cancers in the European Prospective Investigation into Cancer and Nutrition (EPIC). Wozniak MB, Brennan P, Brenner DR, Overvad K, Olsen A, Tjønneland A, Boutron-Ruault MC, Clavel-Chapelon F, Fagherazzi G, Katzke V, Kühn T, Boeing H, Bergmann MM, Steffen A, Naska A, Trichopoulou A, Trichopoulos D, Saieva C, Grioni S, Panico S, Tumino R, Vineis P, Bueno-de-Mesquita HB, Peeters PH, Hjartåker A, Weiderpass E, Arriola L, Molina-Montes E, Duell EJ, Santiuste C, Alonso de la Torre R, Barricarte Gurrea A, Stocks T, Johansson M, Ljungberg B, Wareham N, Khaw KT, Travis RC, Cross AJ, Murphy N, Riboli E, Scelo G.Int J Cancer. 2015 Oct 15;137(8):1953-66. [Epub 2015

Apr 28]. doi: 10.1002/ijc.29559," eng, 2017. DOI: 10.1016/j.urolonc.2016.12.022. [Online]. Available: https://www.iris.unina.it/handle/11588/673896.2 (visited on 02/13/2025).

[22] Y. Lotan *et al.*, "Renal-cell carcinoma risk estimates based on participants in the prostate, lung, colorectal, and ovarian cancer screening trial and national lung screening trial," *Urologic Oncology: Seminars and Original Investigations*, Seminar on Immunotherapy and Cancer Vaccines, vol. 34, no. 4, 167.e9–167.e16, Apr. 2016. DOI: 10.1016/j.urolonc.2015.10.011. [Online]. Available: https://www.sciencedirect.com/science/article/pii/S1078143915004974 (visited on 02/13/2025).

[23] M. M. Nguyen, I. S. Gill, and L. M. Ellison, "The Evolving Presentation of Renal Carcinoma in the United States: Trends From the Surveillance, Epidemiology, and End Results Program," EN, *Journal of Urology*, Dec. 2006, Publisher: Wolters KluwerPhiladelphia, PA. DOI: 10.1016/j.juro.2006.07.144. [Online]. Available: https://www.auajournals.org/doi/10.1016/j.juro.2006.07.144 (visited on 02/14/2025).

[24] *Combination therapies to outsmart cancer - The Institute of Cancer Research, London*. [Online]. Available: https://www.icr.ac.uk/support-us/our-appeals/combination-treatments (visited on 02/12/2025).

[25] R. B. Mokhtari *et al.*, "Combination therapy in combating cancer," *Oncotarget*, vol. 8, no. 23, pp. 38 022–38 043, Mar. 2017. DOI: 10.18632/oncotarget.16723. [Online]. Available: https://www.ncbi.nlm.nih.gov/pmc/articles/PMC5514969/ (visited on 02/12/2025).

[26] M. Shields, "Chapter 14 - Chemotherapeutics," en, in *Pharmacognosy*, S. Badal and R. Delgoda, Eds., Boston: Academic Press, Jan. 2017, pp. 295–313. DOI: 10.1016/B978-0-12-802104-0.00014-7. [Online]. Available: https://www.sciencedirect.com/science/article/pii/B9780128021040000147 (visited on 02/12/2025).

[27] R. T. Skeel and S. N. Khleif, *Handbook of Cancer Chemotherapy*, en. Lippincott Williams & Wilkins, 2011.

[28] J. Wu, "The Enhanced Permeability and Retention (EPR) Effect: The Significance of the Concept and Methods to Enhance Its Application," *Journal of Personalized Medicine*, vol. 11, no. 8, p. 771, Aug. 2021. DOI: 10.3390/jpm11080771. [Online]. Available: https://www.ncbi.nlm.nih.gov/pmc/articles/PMC8402171/ (visited on 02/12/2025).

[29] M. L. Meistrich, "Effects of chemotherapy and radiotherapy on spermatogenesis in humans," *Fertility and Sterility*, vol. 100, no. 5, pp. 1180–1186, Nov. 2013. DOI: 10.1016/j.fertnstert.2013.08.010. [Online]. Available: https://www.sciencedirect.com/science/article/pii/S0015028213029555 (visited on 02/15/2025).

[30] *Chemotherapy Treats Many Different Types of Cancer | UVA Health*. [Online]. Available: https://uvahealth.com/services/cancer/chemotherapy (visited on 02/12/2025).

[31] M. M. Gonzales Carazas, J. A. Pinto, and F. L. Casado, "Biological bases of cancer immunotherapy," en, *Expert Reviews in Molecular Medicine*, vol. 23, e3, 2021. DOI: 10.1017/erm.2021.5. [Online]. Available: https://www.cambridge.org/core/product/identifier/S1462399421000053/type/journal_article (visited on 02/12/2025).

[32] D. Cao *et al.*, "Opportunities and challenges in targeted therapy and immunotherapy for pancreatic cancer," en, *Expert Reviews in Molecular Medicine*, vol. 23, e21, 2021. DOI: 10.1017/erm.2021.26. [Online]. Available: https://www.cambridge.org/core/product/identifier/S1462399421000260/type/journal_article (visited on 02/12/2025).

[33] I. Mellman, G. Coukos, and G. Dranoff, "Cancer immunotherapy comes of age," en, *Nature*, vol. 480, no. 7378, pp. 480–489, Dec. 2011. DOI: 10.1038/nature10673. [Online]. Available: https://www.nature.com/articles/nature10673 (visited on 02/12/2025).

[34] R. Sullivan *et al.*, "Global cancer surgery: Delivering safe, affordable, and timely cancer surgery," en, *The Lancet Oncology*, vol. 16, no. 11, pp. 1193–1224, Sep. 2015. DOI: 10.1016/S1470-2045(15)00223-5. [Online]. Available: https:

//www.sciencedirect.com/science/article/pii/S1470204515002235 (visited on 02/12/2025).

[35] *Treatments - Surgery*, en-US. [Online]. Available: https://digestivecancers.eu/colorectal-treatments-surgery/ (visited on 02/12/2025).

[36] Y. Lemoigne and A. Caner, *Radiotherapy and Brachytherapy*, en. Springer Science & Business Media, Sep. 2009.

[37] G. Borrego-Soto, R. Ortiz-López, and A. Rojas-Martínez, "Ionizing radiation-induced DNA injury and damage detection in patients with breast cancer," *Genetics and Molecular Biology*, vol. 38, no. 4, pp. 420–432, 2015. DOI: 10.1590/S1415-475738420150019. [Online]. Available: https://www.ncbi.nlm.nih.gov/pmc/articles/PMC4763322/ (visited on 02/12/2025).

[38] E. Podgorsak, *Radiation Oncology Physics: A Handbook for Teachers and Students*, English. International Atomic Energy Agency.

[39] P. G. Prasanna *et al.*, "Normal tissue protection for improving radiotherapy: Where are the Gaps?" *Translational cancer research*, vol. 1, no. 1, pp. 35–48, Jun. 2012. [Online]. Available: https://www.ncbi.nlm.nih.gov/pmc/articles/PMC3411185/ (visited on 02/12/2025).

[40] A. Pilar, M. Gupta, S. Ghosh Laskar, and S. Laskar, "Intraoperative radiotherapy: Review of techniques and results," *ecancermedicalscience*, vol. 11, p. 750, Jun. 2017. DOI: 10.3332/ecancer.2017.750. [Online]. Available: https://www.ncbi.nlm.nih.gov/pmc/articles/PMC5493441/ (visited on 02/12/2025).

[41] M. Ahmed *et al.*, "Image-guided Tumor Ablation: Standardization of Terminology and Reporting Criteria—A 10-Year Update," *Radiology*, vol. 273, no. 1, pp. 241–260, Oct. 2014, Publisher: Radiological Society of North America. DOI: 10.1148/radiol.14132958. [Online]. Available: https://pubs.rsna.org/doi/abs/10.1148/radiol.14132958 (visited on 03/27/2025).

[42] S. N. Goldberg *et al.*, "Image-guided Tumor Ablation: Proposal for Standardization of Terms and Reporting Criteria," *Radiology*, vol. 228, no. 2, pp. 335–345, Aug. 2003, Publisher: Radiological Society of North America. DOI: 10.1148/radiol.2282021787. [Online]. Available: https://pubs.rsna.org/doi/abs/10.1148/radiol.2282021787 (visited on 03/27/2025).

[43] D. J. Breen and R. Lencioni, "Image-guided ablation of primary liver and renal tumours," en, *Nature Reviews Clinical Oncology*, vol. 12, no. 3, pp. 175–186, Mar. 2015, Publisher: Nature Publishing Group. DOI: 10.1038/nrclinonc.2014.237. [Online]. Available: https://www.nature.com/articles/nrclinonc.2014.237 (visited on 02/13/2025).

[44] postDICOM, *Medical Imaging Types and Modalities*, en. [Online]. Available: https://www.postdicom.com/en/blog/medical-imaging-types-and-modalities (visited on 02/12/2025).

[45] *X-Ray Physics: X-Ray Interaction with Matter, X-Ray Contrast, and Dose - XRay-Physics*. [Online]. Available: http://xrayphysics.com/attenuation.html (visited on 02/12/2025).

[46] *Read this Imaging Article by Scott Secrest*. [Online]. Available: https://www.vetfolio.com/learn/article/basic-principles-of-ultrasonography (visited on 03/20/2025).

[47] *MRI Basics*. [Online]. Available: https://case.edu/med/neurology/NR/MRI%20Basics.htm (visited on 02/12/2025).

[48] *Open Medscience*, en-GB, Mar. 2023. [Online]. Available: https://openmedscience.com/medical-imaging-modalities/ (visited on 02/12/2025).

[49] C. Imaging, *History of the CT Scan | Catalina Imaging*, en-US, Mar. 2019. [Online]. Available: https://catalinaimaging.com/history-ct-scan/ (visited on 02/12/2025).

[50] J. Abdullah *et al.*, "GammaScorpion: Mobile gamma-ray tomography system for early detection of basal stem rot in oil palm plantations," *Optical Engineering*, vol. 52, p. 036 502, Mar. 2013. DOI: 10.1117/1.OE.52.3.036502.

[51] *Thermionic Emission - an overview | ScienceDirect Topics*. [Online]. Available: https://www.sciencedirect.com/topics/earth-and-planetary-sciences/thermionic-emission (visited on 02/12/2025).

[52] *X-ray Generation, Pictorial Guide [Bremsstrahlung, Characteristic] • How Radiology Works*. [Online]. Available: https://howradiologyworks.com/xrayproduction/ (visited on 02/12/2025).

[53] M. M. Nadrljanski, *Anode (x-ray tube) | Radiology Reference Article | Radiopaedia.org*, en-US. DOI: 10.53347/rID-8178. [Online]. Available: https://radiopaedia.org/articles/anode-x-ray-tube (visited on 02/12/2025).

[54] J. Yeung, *Bremsstrahlung radiation | Radiology Reference Article | Radiopaedia.org*, en-US. DOI: 10.53347/rID-14248. [Online]. Available: https://radiopaedia.org/articles/bremsstrahlung-radiation (visited on 02/12/2025).

[55] *X-rays*. [Online]. Available: http://hyperphysics.phy-astr.gsu.edu/hbase/quantum/xrayc.html (visited on 02/12/2025).

[56] *5.6: Bohr's Atomic Model*, en, Jun. 2016. [Online]. Available: https://chem.libretexts.org/Bookshelves/Introductory_Chemistry/Introductory_Chemistry_(CK-12)/05%3A_Electrons_in_Atoms/5.06%3A_Bohr's_Atomic_Model (visited on 02/12/2025).

[57] M. Tivnan, W. Wang, G. Gang, and J. W. Stayman, *Design of Spatial-Spectral Filters for CT Material Decomposition*, arXiv:2010.07483 [physics], Oct. 2020. [Online]. Available: http://arxiv.org/abs/2010.07483 (visited on 02/12/2025).

[58] *Bremsstrahlung - an overview | ScienceDirect Topics*. [Online]. Available: https://www.sciencedirect.com/topics/chemistry/bremsstrahlung (visited on 02/12/2025).

[59] K. S. Gleisner and M. Ljungberg, "Patient-specific whole-body attenuation correction maps from a CT system for conjugate-view-based activity quantification: Method development and evaluation," eng, *Cancer Biotherapy & Radiopharmaceuticals*, vol. 27, no. 10, pp. 652–664, Dec. 2012. DOI: 10.1089/cbr.2011.1082.

[60] A. Malusek, "Calculation of scatter in cone beam CT," en, Doctoral, Linkoping University.

[61] L. F. Pires *et al.*, "Gamma ray attenuation for determining soil density: Laboratory experiments for Environmental Physics and Engineering courses," en, DOI: https://doi.org/10.1590/1806-9126-RBEF-2019-0340. [Online]. Available: https://www.scielo.br/j/rbef/a/qh3s6C7VmhRKC5DpL4dxmzt/?format=html&lang=en (visited on 03/19/2025).

[62] *Image Reconstruction Techniques*. [Online]. Available: https://www.imagewisely.org/Imaging-Modalities/Computed-Tomography/Image-Reconstruction-Techniques (visited on 02/12/2025).

[63] J. Beatty, "The Radon Transform and the Mathematics of Medical Imaging," en,

[64] T. D. DenOtter and J. Schubert, "Hounsfield Unit," eng, in *StatPearls*, Treasure Island (FL): StatPearls Publishing, 2023. [Online]. Available: http://www.ncbi.nlm.nih.gov/books/NBK547721/ (visited on 02/12/2025).

[65] *Earth's magnetic field*, en, Page Version ID: 1279526868, Mar. 2025. [Online]. Available: https://en.wikipedia.org/w/index.php?title=Earth%27s_magnetic_field&oldid=1279526868 (visited on 04/05/2025).

[66] *Nobel Prize in Physiology or Medicine 2003*, en-US. [Online]. Available: https://www.nobelprize.org/prizes/medicine/2003/press-release/ (visited on 04/05/2025).

[67] M. Lax and D. F. Nelson, "Maxwell equations in material form," *Physical Review B*, vol. 13, no. 4, pp. 1777–1784, Feb. 1976, Publisher: American Physical Society. DOI: 10.1103/PhysRevB.13.1777. [Online]. Available: https://link.aps.org/doi/10.1103/PhysRevB.13.1777 (visited on 04/07/2025).

[68] M. Manso Jimeno, J. T. Vaughan, and S. Geethanath, "Superconducting magnet designs and MRI accessibility: A review," en, *NMR in Biomedicine*, vol. 36, no. 9, e4921, 2023, _eprint: https://onlinelibrary.wiley.com/doi/pdf/10.1002/nbm.4921. DOI: 10.1002/nbm.4921. [Online]. Available: https://onlinelibrary.wiley.com/doi/abs/10.1002/nbm.4921 (visited on 04/07/2025).

[69] E. Blink, *MRI: Physics For anyone who has not a degree in physics*, en. UK. [Online]. Available: https://learnak.io/wp-content/uploads/2023/02/mri-physics-uk.pdf (visited on 04/07/2025).

[70] D. B. Plewes and W. Kucharczyk, "Physics of MRI: A primer," en, *Journal of Magnetic Resonance Imaging*, vol. 35, no. 5, pp. 1038–1054, 2012, _eprint: https://onlinelibrary.wiley.com/doi/pd DOI: 10.1002/jmri.23642. [Online]. Available: https://onlinelibrary.wiley.com/doi/abs/10.1002/jmri.23642 (visited on 04/07/2025).

[71] W. Hinshaw and A. Lent, "An introduction to NMR imaging: From the Bloch equation to the imaging equation," *Proceedings of the IEEE*, vol. 71, no. 3, pp. 338–350, Mar. 1983. DOI: 10.1109/PROC.1983.12592. [Online]. Available: https://ieeexplore.ieee.org/abstract/document/1456860 (visited on 04/07/2025).

[72] *What Is Image Segmentation? | IBM*, en, Sep. 2023. [Online]. Available: https://www.ibm.com/think/topics/image-segmentation (visited on 04/05/2025).

[73] F. Yang, F. Wang, P. Dong, and B. Wang, "HCA-former: Hybrid Convolution Attention Transformer for 3D Medical Image Segmentation," *Biomedical Signal Processing and Control*, vol. 90, p. 105 834, Apr. 2024. DOI: 10.1016/j.bspc.2023.105834. [Online]. Available: https://www.sciencedirect.com/science/article/pii/S1746809423012673 (visited on 02/14/2025).

[74] N. Sharma and L. M. Aggarwal, "Automated medical image segmentation techniques," *Journal of Medical Physics / Association of Medical Physicists of India*, vol. 35, no. 1, pp. 3–14, 2010. DOI: 10.4103/0971-6203.58777. [Online]. Available: https://www.ncbi.nlm.nih.gov/pmc/articles/PMC2825001/ (visited on 04/05/2025).

[75] Y. Jiang *et al.*, "Quo vadis artificial intelligence?" En, *Discover Artificial Intelligence*, vol. 2, no. 1, pp. 1–19, Mar. 2022, Number: 1 Publisher: Springer. DOI: 10.1007/s44163-022-00022-8. [Online]. Available: https://link.springer.com/article/10.1007/s44163-022-00022-8 (visited on 04/09/2025).

[76] B. Mahesh, "Machine Learning Algorithms - A Review," *International Journal of Science and Research (IJSR)*, vol. 9, no. 1, pp. 381–386, Jan. 2020. DOI: 10.21275/ART20203995. [Online]. Available: https://www.ijsr.net/archive/v9i1/ART20203995.pdf (visited on 04/09/2025).

[77] N. Zhang, S.-L. Shen, A. Zhou, and Y.-S. Xu, "Investigation on Performance of Neural Networks Using Quadratic Relative Error Cost Function," *IEEE Access*, vol. 7, pp. 106 642–106 652, 2019. DOI: 10.1109/ACCESS.2019.2930520. [Online]. Available: https://ieeexplore.ieee.org/abstract/document/8769865 (visited on 04/09/2025).

[78] K. Sharifani and M. Amini, *Machine Learning and Deep Learning: A Review of Methods and Applications*, en, SSRN Scholarly Paper, Rochester, NY. [Online].

Available: https://papers.ssrn.com/sol3/papers.cfm?abstract_id=4458723 (visited on 04/09/2025).

[79] S. S. Sengar, A. B. Hasan, S. Kumar, and F. Carroll, "Generative artificial intelligence: A systematic review and applications," En, *Multimedia Tools and Applications*, pp. 1–40, Aug. 2024, Publisher: Springer. DOI: 10.1007/s11042-024-20016-1. [Online]. Available: https://link.springer.com/article/10.1007/s11042-024-20016-1 (visited on 04/10/2025).

[80] R. Gozalo-Brizuela and E. C. Garrido-Merchan, *ChatGPT is not all you need. A State of the Art Review of large Generative AI models*, arXiv:2301.04655 [cs], Jan. 2023. DOI: 10.48550/arXiv.2301.04655. [Online]. Available: http://arxiv.org/abs/2301.04655 (visited on 04/09/2025).

[81] O. Ronneberger, P. Fischer, and T. Brox, "U-Net: Convolutional Networks for Biomedical Image Segmentation," en, Nov. 2015. DOI: 10.1007/978-3-319-24574-4_28. [Online]. Available: https://link.springer.com/chapter/10.1007/978-3-319-24574-4_28 (visited on 04/09/2025).

[82] F. Milletari, N. Navab, and S.-A. Ahmadi, "V-Net: Fully Convolutional Neural Networks for Volumetric Medical Image Segmentation," in *2016 Fourth International Conference on 3D Vision (3DV)*, Oct. 2016, pp. 565–571. DOI: 10.1109/3DV.2016.79. [Online]. Available: https://ieeexplore.ieee.org/abstract/document/7785132 (visited on 04/10/2025).

[83] M. J. Trimpl *et al.*, "Beyond automatic medical image segmentation—the spectrum between fully manual and fully automatic delineation," en, *Physics in Medicine & Biology*, vol. 67, no. 12, 12TR01, Jun. 2022, Publisher: IOP Publishing. DOI: 10.1088/1361-6560/ac6d9c. [Online]. Available: https://dx.doi.org/10.1088/1361-6560/ac6d9c (visited on 04/28/2025).

[84] D. L. Pham, C. Xu, and J. L. Prince, "Current Methods in Medical Image Segmentation," en, *Annual Review of Biomedical Engineering*, vol. 2, no. 1, pp. 315–337, Aug. 2000. DOI: 10.1146/annurev.bioeng.2.1.315. [Online]. Available: http://www.annualreviews.org/doi/10.1146/annurev.bioeng.2.1.315 (visited on 04/28/2025).

[85] N. Otsu, "A Threshold Selection Method from Gray-Level Histograms," *IEEE Transactions on Systems, Man, and Cybernetics*, vol. 9, no. 1, pp. 62–66, Jan. 1979. DOI: 10.1109/TSMC.1979.4310076. [Online]. Available: https://ieeexplore.ieee.org/document/4310076 (visited on 04/27/2025).

[86] M. Gudmundsson, E. El-Kwae, and M. Kabuka, "Edge detection in medical images using a genetic algorithm," *IEEE Transactions on Medical Imaging*, vol. 17, no. 3, pp. 469–474, Jun. 1998. DOI: 10.1109/42.712136. [Online]. Available: https://ieeexplore.ieee.org/abstract/document/712136 (visited on 04/28/2025).

[87] R. Song, Z. Zhang, and H. Liu, "Edge connection based Canny edge detection algorithm," En, *Pattern Recognition and Image Analysis*, vol. 27, no. 4, pp. 740–747, Dec. 2017, Number: 4 Publisher: Springer. DOI: 10.1134/S1054661817040162. [Online]. Available: https://link.springer.com/article/10.1134/S1054661817040162 (visited on 04/28/2025).

[88] Z. Zhao, H. Chen, and L. Wang, "A Coarse-to-Fine Framework for the 2021 Kidney and Kidney Tumor Segmentation Challenge," en, Mar. 2022. DOI: 10.1007/978-3-030-98385-7_8. [Online]. Available: https://link.springer.com/chapter/10.1007/978-3-030-98385-7_8 (visited on 09/27/2024).

[89] C. Chen and R. Zhang, "An Ensemble of 2.5D ResUnet Based Models for Segmentation of Kidney and Masses," en, Mar. 2024. DOI: 10.1007/978-3-031-54806-2_7. [Online]. Available: https://link.springer.com/chapter/10.1007/978-3-031-54806-2_7 (visited on 11/04/2024).

[90] F. Isensee *et al.*, "nnU-Net: A self-configuring method for deep learning-based biomedical image segmentation," en, *Nature Methods*, vol. 18, no. 2, pp. 203–211, Feb. 2021, Publisher: Nature Publishing Group. DOI: 10.1038/s41592-020-01008-z. [Online]. Available: https://www.nature.com/articles/s41592-020-01008-z (visited on 09/27/2024).

[91] *An Ensemble of 3D U-Net Based Models for Segmentation of Kidney and Masses in CT Scans | SpringerLink*. [Online]. Available: https://link.springer.com/chapter/10.1007/978-3-030-98385-7_14 (visited on 11/04/2024).

[92] L. Qian, L. Luo, Y. Zhong, and D. Zhong, "A Hybrid Network Based on nnU-Net and Swin Transformer for Kidney Tumor Segmentation," en, Mar. 2024. DOI: 10.

1007/978-3-031-54806-2_5. [Online]. Available: https://link.springer.com/chapter/10.1007/978-3-031-54806-2_5 (visited on 11/04/2024).

[93] S. Lee, H. Won, and Y. Lee, "Two-Stage Segmentation and Ensemble Modeling: Kidney Tumor Analysis in CT Images," en, Mar. 2024. DOI: 10.1007/978-3-031-54806-2_9. [Online]. Available: https://link.springer.com/chapter/10.1007/978-3-031-54806-2_9 (visited on 11/04/2024).

[94] T. Li *et al.*, "Genetic Algorithm Enhanced nnU-Net for the MICCAI KiTS23 Challenge," en, Mar. 2024. DOI: 10.1007/978-3-031-54806-2_11. [Online]. Available: https://link.springer.com/chapter/10.1007/978-3-031-54806-2_11 (visited on 11/04/2024).

[95] Z. Li, Y. Peng, and Z. Zhang, "Two-Stage Segmentation Framework with Parallel Decoders for the Kidney and Kidney Tumor Segmentation," en, Mar. 2024. DOI: 10.1007/978-3-031-54806-2_12. [Online]. Available: https://link.springer.com/chapter/10.1007/978-3-031-54806-2_12 (visited on 11/04/2024).

[96] A. Sinha and J. Dolz, "Multi-Scale Self-Guided Attention for Medical Image Segmentation," *IEEE Journal of Biomedical and Health Informatics*, vol. 25, no. 1, pp. 121–130, Jan. 2021, Conference Name: IEEE Journal of Biomedical and Health Informatics. DOI: 10.1109/JBHI.2020.2986926. [Online]. Available: https://ieeexplore.ieee.org/document/9066969 (visited on 11/04/2024).

[97] Z. Gu *et al.*, "CE-Net: Context Encoder Network for 2D Medical Image Segmentation," *IEEE Transactions on Medical Imaging*, vol. 38, no. 10, pp. 2281–2292, Oct. 2019, Conference Name: IEEE Transactions on Medical Imaging. DOI: 10.1109/TMI.2019.2903562. [Online]. Available: https://ieeexplore.ieee.org/document/8662594 (visited on 11/04/2024).

[98] M. S. B. Islam *et al.*, "Classification and segmentation of kidney MRI images for chronic kidney disease detection," *Computers and Electrical Engineering*, vol. 119, p. 109 613, Nov. 2024. DOI: 10.1016/j.compeleceng.2024.109613. [Online]. Available: https://www.sciencedirect.com/science/article/pii/S0045790624005408 (visited on 11/04/2024).

[99] A. Shaker *et al.*, *UNETR++: Delving into Efficient and Accurate 3D Medical Image Segmentation*, arXiv:2212.04497, May 2024. DOI: 10.48550/arXiv.2212.04497. [Online]. Available: http://arxiv.org/abs/2212.04497 (visited on 11/04/2024).

[100] S. Nema, A. Dudhane, S. Murala, and S. Naidu, "RescueNet: An unpaired GAN for brain tumor segmentation," *Biomedical Signal Processing and Control*, vol. 55, p. 101 641, Jan. 2020. DOI: 10.1016/j.bspc.2019.101641. [Online]. Available: https://www.sciencedirect.com/science/article/pii/S1746809419302228 (visited on 11/04/2024).

[101] *Colorectal cancer prediction via histopathology segmentation using DC-GAN and VAE-GAN | EAI Endorsed Transactions on Pervasive Health and Technology*. [Online]. Available: https://publications.eai.eu/index.php/phat/article/view/5395 (visited on 11/04/2024).

[102] M. D. Cirillo, D. Abramian, and A. Eklund, "Vox2Vox: 3D-GAN for Brain Tumour Segmentation," en, Mar. 2021. DOI: 10.1007/978-3-030-72084-1_25. [Online]. Available: https://link.springer.com/chapter/10.1007/978-3-030-72084-1_25 (visited on 11/16/2024).

[103] K. Li, L. Kong, and Y. Zhang, "3D U-Net Brain Tumor Segmentation Using VAE Skip Connection," in *2020 IEEE 5th International Conference on Image, Vision and Computing (ICIVC)*, Jul. 2020, pp. 97–101. DOI: 10.1109/ICIVC50857.2020.9177441. [Online]. Available: https://ieeexplore.ieee.org/document/9177441 (visited on 11/04/2024).

[104] *KiTS19 - Grand Challenge*, en. [Online]. Available: https://kits19.grand-challenge.org/ (visited on 03/03/2025).

[105] *The 2021 Kidney Tumor Segmentation Challenge*, en. [Online]. Available: https://kits-challenge.org/kits21/ (visited on 03/03/2025).

[106] *KiTS23 | The 2023 Kidney Tumor Segmentation Challenge*. [Online]. Available: https://kits-challenge.org/kits23/ (visited on 03/03/2025).

[107] *C4KC-KITS*, en-US. [Online]. Available: https://www.cancerimagingarchive.net/collection/c4kc-kits/ (visited on 03/03/2025).

[108] N. Heller *et al.*, *The KiTS19 Challenge Data: 300 Kidney Tumor Cases with Clinical Context, CT Semantic Segmentations, and Surgical Outcomes*, arXiv:1904.00445 [q-bio], Mar. 2020. DOI: 10.48550/arXiv.1904.00445. [Online]. Available: http://arxiv.org/abs/1904.00445 (visited on 04/07/2025).

[109] *Anatomy of the Urinary System*, en, Apr. 2025. [Online]. Available: https://www.hopkinsmedicine.org/health/wellness-and-prevention/anatomy-of-the-urinary-system (visited on 04/09/2025).

[110] A. Myronenko, D. Yang, Y. He, and D. Xu, "Automated 3D Segmentation of Kidneys and Tumors in MICCAI KiTS 2023 Challenge," en, Mar. 2024. DOI: 10.1007/978-3-031-54806-2_1. [Online]. Available: https://link.springer.com/chapter/10.1007/978-3-031-54806-2_1 (visited on 04/29/2025).

[111] *Exploring 3D U-Net Training Configurations and Post-processing Strategies for the MICCAI 2023 Kidney and Tumor Segmentation Challenge | SpringerLink*. [Online]. Available: https://link.springer.com/chapter/10.1007/978-3-031-54806-2_2 (visited on 11/04/2024).

[112] Y. George, "A Coarse-to-Fine 3D U-Net Network for Semantic Segmentation of Kidney CT Scans," en, Mar. 2022. DOI: 10.1007/978-3-030-98385-7_18. [Online]. Available: https://link.springer.com/chapter/10.1007/978-3-030-98385-7_18 (visited on 04/29/2025).

[113] S. Liu and B. Han, "Dynamic Resolution Network for Kidney Tumor Segmentation," en, Mar. 2024. DOI: 10.1007/978-3-031-54806-2_3. [Online]. Available: https://link.springer.com/chapter/10.1007/978-3-031-54806-2_3 (visited on 04/29/2025).

[114] G. Stoica, M. Breaban, and V. Barbu, "Analyzing Domain Shift When Using Additional Data for the MICCAI KiTS23 Challenge," en, Mar. 2024. DOI: 10.1007/978-3-031-54806-2_4. [Online]. Available: https://link.springer.com/chapter/10.1007/978-3-031-54806-2_4 (visited on 04/29/2025).

[115] Z. Salahuddin, S. Kuang, P. Lambin, and H. C. Woodruff, "Leveraging Uncertainty Estimation for Segmentation of Kidney, Kidney Tumor and Kidney Cysts," en, Mar. 2024. DOI: 10.1007/978-3-031-54806-2_6. [Online]. Available: https:

//link.springer.com/chapter/10.1007/978-3-031-54806-2_6 (visited on 04/29/2025).

[116] J. Michaud, T. W. Arega, and S. Bricq, "Using Uncertainty Information for Kidney Tumor Segmentation," en, Mar. 2024. DOI: 10.1007/978-3-031-54806-2_8. [Online]. Available: https://link.springer.com/chapter/10.1007/978-3-031-54806-2_8 (visited on 04/29/2025).

Appendix A

JHU naming change

Table A.1: Name correspondence in JHU dataset between JHU given name and renaming for nnU-Net use.

Name given by JHU	Renamed as
JHU_0001/pre	JHU_000_0000
JHU_0001/pre_A	JHU_001_0000
JHU_0001/pre_V	JHU_002_0000
JHU_0002/pre	JHU_003_0000
JHU_0003/pre	JHU_004_0000
JHU_0004/pre	JHU_005_0000
JHU_0005/pre	JHU_006_0000
JHU_0006/pre	JHU_007_0000
JHU_0006/pre_A	JHU_008_0000
JHU_0007/pre	JHU_009_0000
JHU_0008/pre	JHU_010_0000
JHU_0009/pre	JHU_011_0000
JHU_0010/pre_1	JHU_012_0000
JHU_0010/pre_2	JHU_013_0000
JHU_0010/pre_A_1	JHU_014_0000
JHU_0010/pre_A_1 2	JHU_015_0000
JHU_0010/pre_V_1	JHU_016_0000

Table A.1: Name correspondence in JHU dataset between JHU given name and renaming for nnU-Net use.

Name given by JHU	**Renamed as**
JHU_0010/pre_V_2	JHU_017_0000
JHU_0011/pre	JHU_018_0000
JHU_0012/pre	JHU_019_0000
JHU_0012/pre_A	JHU_020_0000
JHU_0012/pre_V	JHU_021_0000
JHU_0013/pre	JHU_022_0000
JHU_0014/pre_1	JHU_023_0000
JHU_0014/pre_1_A	JHU_024_0000
JHU_0014/pre_1_V	JHU_025_0000
JHU_0014/pre_2	JHU_026_0000
JHU_0014/pre_2_A	JHU_027_0000
JHU_0014/pre_2_V	JHU_028_0000
JHU_0015/pre	JHU_029_0000
JHU_0015/pre 2	JHU_030_0000
JHU_0015/pre 3	JHU_031_0000
JHU_0015/pre 4	JHU_032_0000
JHU_0015/pre 5	JHU_033_0000
JHU_0015/pre 6	JHU_034_0000
JHU_0015/pre_A	JHU_035_0000
JHU_0015/pre_A 2	JHU_036_0000
JHU_0015/pre_A 3	JHU_037_0000
JHU_0015/pre_A 4	JHU_038_0000
JHU_0015/pre_A 5	JHU_039_0000
JHU_0015/pre_V	JHU_040_0000
JHU_0015/pre_V 2	JHU_041_0000
JHU_0015/pre_V 3	JHU_042_0000
JHU_0016/pre_1	JHU_043_0000
JHU_0016/pre_1_A	JHU_044_0000

Table A.1: Name correspondence in JHU dataset between JHU given name and renaming for nnU-Net use.

Name given by JHU	**Renamed as**
JHU_0016/pre_1_V	JHU_045_0000
JHU_0016/pre_2	JHU_046_0000
JHU_0016/pre_2_A	JHU_047_0000
JHU_0016/pre_2_V	JHU_048_0000
JHU_0017/pre	JHU_049_0000
JHU_0017/pre_A	JHU_050_0000
JHU_0017/pre_V	JHU_051_0000
JHU_0018/pre	JHU_052_0000
JHU_0018/pre_A	JHU_053_0000
JHU_0018/pre_V	JHU_054_0000
JHU_0019/pre	JHU_055_0000
JHU_0020/pre	JHU_056_0000
JHU_0020/pre_A	JHU_057_0000
JHU_0020/pre_V	JHU_058_0000
JHU_0021/pre	JHU_059_0000
JHU_0021/pre_A	JHU_060_0000
JHU_0021/pre_V	JHU_061_0000
JHU_0022/pre	JHU_062_0000
JHU_0022/pre_A	JHU_063_0000
JHU_0022/pre_V	JHU_064_0000
JHU_0023/pre	JHU_065_0000
JHU_0023/pre_A	JHU_066_0000
JHU_0024/pre	JHU_067_0000
JHU_0024/pre_A	JHU_068_0000
JHU_0024/pre_V	JHU_069_0000
JHU_0025/pre	JHU_070_0000
JHU_0027/pre_2	JHU_071_0000
JHU_0027/pre_V_1	JHU_072_0000

Table A.1: Name correspondence in JHU dataset between JHU given name and renaming for nnU-Net use.

Name given by JHU	**Renamed as**
JHU_0027/pre_V_1 2	JHU_073_0000
JHU_0028/pre_V	JHU_074_0000
JHU_0029/pre	JHU_075_0000
JHU_0029/pre_A	JHU_076_0000
JHU_0029/pre_V	JHU_077_0000
JHU_0030/pre	JHU_078_0000
JHU_0030/pre_A	JHU_079_0000
JHU_0030/pre_V	JHU_080_0000
JHU_0032/pre	JHU_081_0000
JHU_0033/pre	JHU_082_0000
JHU_0033/pre_A	JHU_083_0000
JHU_0033/pre_V	JHU_084_0000
JHU_0034/pre_A	JHU_085_0000
JHU_0035/pre_A	JHU_086_0000
JHU_0035/pre_V	JHU_087_0000
JHU_0036/pre	JHU_088_0000
JHU_0036/pre_A	JHU_089_0000
JHU_0036/pre_V	JHU_090_0000
JHU_0037/pre	JHU_091_0000
JHU_0037/pre_A	JHU_092_0000
JHU_0037/pre_V	JHU_093_0000
JHU_0038/pre	JHU_094_0000
JHU_0039/pre	JHU_095_0000
JHU_0040/Pre	JHU_096_0000
JHU_0040/Pre_A	JHU_097_0000
JHU_0040/Pre_V	JHU_098_0000
JHU_0041/pre	JHU_099_0000
JHU_0041/pre_A	JHU_100_0000

Table A.1: Name correspondence in JHU dataset between JHU given name and renaming for nnU-Net use.

Name given by JHU	**Renamed as**
JHU_0041/pre_V	JHU_101_0000
JHU_0042/pre	JHU_102_0000
JHU_0042/pre_A	JHU_103_0000
JHU_0042/pre_V	JHU_104_0000
JHU_0043/pre_V	JHU_105_0000
JHU_0044/pre	JHU_106_0000
JHU_0045/pre	JHU_107_0000
JHU_0046/pre	JHU_108_0000
JHU_0047/pre	JHU_109_0000
JHU_0047/pre_A	JHU_110_0000
JHU_0047/pre_V	JHU_111_0000
JHU_0048/pre	JHU_112_0000
JHU_0048/pre_A	JHU_113_0000
JHU_0049/Pre_A	JHU_114_0000
JHU_0049/pre	JHU_115_0000
JHU_0049/pre_V	JHU_116_0000
JHU_0050/pre	JHU_117_0000
JHU_0050/pre_A	JHU_118_0000
JHU_0050/pre_V	JHU_119_0000
JHU_0051/pre	JHU_120_0000
JHU_0052/pre	JHU_121_0000
JHU_0053/pre_A	JHU_122_0000
JHU_0054/pre	JHU_123_0000
JHU_0055/pre	JHU_124_0000
JHU_0056/pre	JHU_125_0000
JHU_0056/pre_A	JHU_126_0000
JHU_0056/pre_V	JHU_127_0000
JHU_0057/pre	JHU_128_0000

Table A.1: Name correspondence in JHU dataset between JHU given name and renaming for nnU-Net use.

Name given by JHU	**Renamed as**
JHU_0058/pre_V	JHU_129_0000
JHU_0059/pre	JHU_130_0000
JHU_0059/pre_A	JHU_131_0000
JHU_0059/pre_V	JHU_132_0000
JHU_0060/pre	JHU_133_0000
JHU_0060/pre_A	JHU_134_0000
JHU_0060/pre_V	JHU_135_0000
JHU_0061/pre	JHU_136_0000
JHU_0062/pre	JHU_137_0000
JHU_0063/pre	JHU_138_0000
JHU_0063/pre_A	JHU_139_0000
JHU_0063/pre_V	JHU_140_0000
JHU_0064/pre	JHU_141_0000
JHU_0065/pre	JHU_142_0000
JHU_0066/pre	JHU_143_0000
JHU_0067/pre_1	JHU_144_0000
JHU_0067/pre_2	JHU_145_0000
JHU_0068/pre_1	JHU_146_0000
JHU_0068/pre_1_A	JHU_147_0000
JHU_0068/pre_1_V	JHU_148_0000
JHU_0068/pre_2	JHU_149_0000
JHU_0068/pre_2_A	JHU_150_0000
JHU_0068/pre_2_V	JHU_151_0000
JHU_0069/pre	JHU_152_0000
JHU_0069/pre_A	JHU_153_0000
JHU_0069/pre_V	JHU_154_0000
JHU_0070/pre	JHU_155_0000
JHU_0071/pre_1	JHU_156_0000

Table A.1: Name correspondence in JHU dataset between JHU given name and renaming for nnU-Net use.

Name given by JHU	**Renamed as**
JHU_0071/pre_1_A	JHU_157_0000
JHU_0071/pre_1_V	JHU_158_0000
JHU_0071/pre_2	JHU_159_0000
JHU_0071/pre_2_A	JHU_160_0000
JHU_0071/pre_2_V	JHU_161_0000
JHU_0072/pre	JHU_162_0000
JHU_0073/pre	JHU_163_0000
JHU_0074/pre_1	JHU_164_0000
JHU_0074/pre_2	JHU_165_0000
JHU_0074/pre_2_A	JHU_166_0000
JHU_0074/pre_2_V	JHU_167_0000
JHU_0075/pre	JHU_168_0000
JHU_0076/pre	JHU_169_0000
JHU_0077/pre	JHU_170_0000
JHU_0077/pre_A	JHU_171_0000
JHU_0077/pre_V	JHU_172_0000
JHU_0078/Pre	JHU_173_0000
JHU_0079/pre	JHU_174_0000
JHU_0079/pre_A	JHU_175_0000
JHU_0079/pre_V	JHU_176_0000
JHU_0080/pre	JHU_177_0000
JHU_0082/pre_T1C	JHU_178_0000
JHU_0082/pre_T2	JHU_179_0000
JHU_0083/pre	JHU_180_0000
JHU_0084/pre_A	JHU_181_0000
JHU_0084/pre_V	JHU_182_0000
JHU_0085/pre	JHU_183_0000
JHU_0085/pre_A	JHU_184_0000

Table A.1: Name correspondence in JHU dataset between JHU given name and renaming for nnU-Net use.

Name given by JHU	**Renamed as**
JHU_0085/pre_V	JHU_185_0000
JHU_0086/pre	JHU_186_0000
JHU_0086/pre_A	JHU_187_0000
JHU_0086/pre_V	JHU_188_0000
JHU_0087/pre	JHU_189_0000
JHU_0087/pre_A	JHU_190_0000
JHU_0087/pre_V	JHU_191_0000
JHU_0088/pre	JHU_192_0000
JHU_0088/pre_A	JHU_193_0000
JHU_0088/pre_V	JHU_194_0000
JHU_0089/pre	JHU_195_0000
JHU_0089/pre_A	JHU_196_0000
JHU_0089/pre_V	JHU_197_0000
JHU_0090/pre_A	JHU_198_0000
JHU_0091/pre_V	JHU_199_0000
JHU_0092/pre	JHU_200_0000
JHU_0093/pre	JHU_201_0000
JHU_0093/pre_A	JHU_202_0000
JHU_0094/pre_A	JHU_203_0000
JHU_0095/pre	JHU_204_0000
JHU_0095/pre_A	JHU_205_0000
JHU_0095/pre_V	JHU_206_0000
JHU_0096/pre	JHU_207_0000
JHU_0096/pre_A	JHU_208_0000
JHU_0096/pre_V	JHU_209_0000
JHU_0097/pre_A	JHU_210_0000
JHU_0098/pre	JHU_211_0000
JHU_0098/pre_A	JHU_212_0000

Table A.1: Name correspondence in JHU dataset between JHU given name and renaming for nnU-Net use.

Name given by JHU	**Renamed as**
JHU_0098/pre_V	JHU_213_0000
JHU_0099/pre_A	JHU_214_0000
JHU_0099/pre_V	JHU_215_0000
JHU_0100/pre	JHU_216_0000
JHU_0101/Pre_2	JHU_217_0000
JHU_0101/Pre_2 2	JHU_218_0000
JHU_0101/Pre_A_2	JHU_219_0000
JHU_0101/Pre_A_2 2	JHU_220_0000
JHU_0101/Pre_V_2	JHU_221_0000
JHU_0101/Pre_V_2 2	JHU_222_0000
JHU_0101/pre_1	JHU_223_0000
JHU_0101/pre_A_1	JHU_224_0000
JHU_0101/pre_V_1	JHU_225_0000
JHU_0102/Pre	JHU_226_0000
JHU_0102/Pre_A	JHU_227_0000
JHU_0102/Pre_V	JHU_228_0000
JHU_0103/Pre	JHU_229_0000